International Journal for Numerical Methods in Engineering

WILEY

RESEARCH ARTICLE

A Virtual Heat Flux Method for Simple and Accurate Neumann Thermal Boundary Imposition in the Material Point Method

Jidu Yu[1,2] | Jidong Zhao[1]

[1]Department of Civil and Environmental Engineering, Hong Kong University of Science and Technology, Hong Kong, China | [2]Department of Civil and Environmental Engineering, University of California, Berkeley, California, USA

Correspondence: Jidu Yu (jyubu@connect.ust.hk) | Jidong Zhao (jzhao@ust.hk)

Received: 12 February 2026 | **Revised:** 11 May 2026 | **Accepted:** 3 June 2026

Keywords: heat transfer | material point method | multiphysics modeling | Neumann boundary condition | nonconforming boundary | virtual heat flux method

ABSTRACT

In the material point method (MPM), accurate enforcement of thermal boundary conditions, particularly convective heat flux boundaries, is crucial for the reliable simulation of thermally coupled multiphysics processes, such as natural heat-convection phenomena on Earth. However, the MPM typically employs a fixed, regular background mesh, whereas material boundaries are often complex and evolve over time. As a result, the boundaries do not generally align with the mesh, making boundary tracking and the consistent application of boundary conditions challenging. This study introduces a virtual heat flux method (VHFM) that enables the simple and accurate imposition of nonconforming heat flux boundary conditions in the MPM. The core idea is to construct a virtual flux field that satisfies the prescribed boundary conditions and converts boundary integrals into volume integrals. This approach eliminates the need for explicit boundary tracking while maintaining ease of implementation and computational efficiency. A unified formulation of the virtual flux field is further developed, allowing the method to be readily extended to general Neumann boundary conditions. Through a series of numerical experiments, the proposed method is shown to achieve high accuracy and convergence across a wide range of nonconforming boundary configurations, including curved, moving, and evolving boundaries. The VHFM provides a potential way for Neumann thermal boundary imposition in thermo-mechanical and other multiphysics MPM frameworks.

1 | Introduction

The material point method (MPM) is a hybrid mesh-particle computational framework that combines the strengths of Lagrangian particles with Eulerian background mesh [1–3]. Compared with the traditional mesh-based finite element method (FEM), the MPM offers substantial advantages for simulating large deformation problems [4, 5]. In recent years,

MPM has been intensively developed to simulate thermo-mechanical [6, 7] and thermo-hydro-mechanical problems [8, 9]. This multiphysics MPM has been widely employed to investigate the thermal effects in various media, such as thermal expansion [7], thermal pressurization [10, 11], thermal softening [12, 13], and shear heating [14], with applications spanning from permafrost melting, hydrate dissociation to geothermal energy extraction [15–17]. While significant progress has been achieved in multiphysics MPM theories, particularly through improvements in time-integration schemes [18, 19] and spatial discretization strategies [20], comparatively limited attention has been devoted to the accurate enforcement of boundary conditions [21].

The accurate imposition of thermal boundary conditions is of fundamental importance for modeling thermally coupled multiphysics problems, as the temperature field directly influences other fields through strong coupling mechanisms [22, 23]. Typical thermal boundary conditions include temperature (i.e., Dirichlet) and heat flux (i.e., Neumann) boundary conditions. While temperature boundary conditions can usually be enforced in MPM with relative ease, the accurate imposition of heat flux boundary conditions is considerably more challenging. Nevertheless, heat flux boundaries are ubiquitous in both natural and engineering systems, as they govern energy exchange processes such as heat transfer between the atmosphere and the Earth's surface, between flowing fluids and solid structures, and across material interfaces [24–26]. In these problems, inaccuracies in the imposed thermal boundary conditions can propagate through the coupled system and significantly affect the hydraulic and mechanical responses.

The difficulty in enforcing heat flux boundary conditions in the MPM primarily arises from the nonconforming relationship between material boundaries and the background grid [27]. In the MPM, a regular and fixed background mesh is typically employed, while materials are represented by a collection of Lagrangian material points whose geometry can be complex and evolve significantly due to large deformation and rotation. As a result, material boundaries are rarely aligned with grid lines, except in highly idealized cases. As illustrated in Figure 1a, the square domain aligned with the grid can be treated accurately, whereas even a simple rotation renders the boundary nonconforming (see Figure 1b). For more complex geometries, such as inclined or curved domains (e.g., Figure 1c–e) or highly irregular shapes (e.g., the Stanford bunny in Figure 1f [28]), boundary alignment with the regular background grid becomes practically impossible. Under such circumstances, directly applying heat flux conditions at grid nodes or material points leads to a loss of accuracy and increased numerical error. Therefore, the development of robust and accurate techniques for imposing heat flux boundary conditions on nonconforming and evolving boundaries remains a critical and unresolved challenge in the MPM simulations.

Although relatively few studies have explicitly focused on the imposition of heat flux boundary conditions in the MPM, existing strategies for enforcing traction boundary conditions provide valuable references [21, 29]. One common approach is to apply boundary conditions directly to material points located near the boundary; however, because material points do not generally coincide with the exact geometric boundary and the effective thickness of the boundary layer used in integration is ill-defined, this method often suffers from limited accuracy and poor convergence [30]. To improve boundary representation, some studies introduce virtual or auxiliary particles in the vicinity of the boundary, which can enhance accuracy but require additional particle generation and tracking procedures, thereby increasing algorithmic complexity and computational cost [31]. Alternatively, moving or adaptive grid techniques have been proposed to better align the background grid with material boundaries, enabling more accurate boundary condition enforcement [32]. Nevertheless, for complex or highly irregular geometries, achieving consistent boundary conformity remains difficult, particularly when regular background meshes are employed, which restricts the robustness and general applicability of these methods.

All of the aforementioned approaches rely on the additional tracking or reconstruction of boundary particles or grids. Although such strategies can improve accuracy, they inevitably increase algorithmic complexity and computational cost. Recently, a virtual stress boundary method was proposed to accurately impose traction boundary conditions in the MPM without explicitly tracking material domain boundaries, offering a promising alternative perspective [27, 33]. Inspired by this idea, the present study introduces a simple and computationally efficient virtual heat flux method (VHFM) for the accurate enforcement of Neumann thermal boundary conditions on nonconforming boundaries. The central concept of the VHFM is to construct a virtual heat flux field on the background grid that reproduces the prescribed boundary heat flux, thereby eliminating the need for explicit boundary tracking or boundary-grid alignment. On this basis, the governing equations are reformulated, and a unified expression for the virtual heat flux field is derived. The method is not only suitable for heat transfer problems but also for thermally coupled multiphysics applications.

The remainder of this paper is organized as follows. Section 2 presents the governing heat transfer equations with heat flux boundary conditions and their discretization within the MPM framework. Section 3 introduces the virtual heat

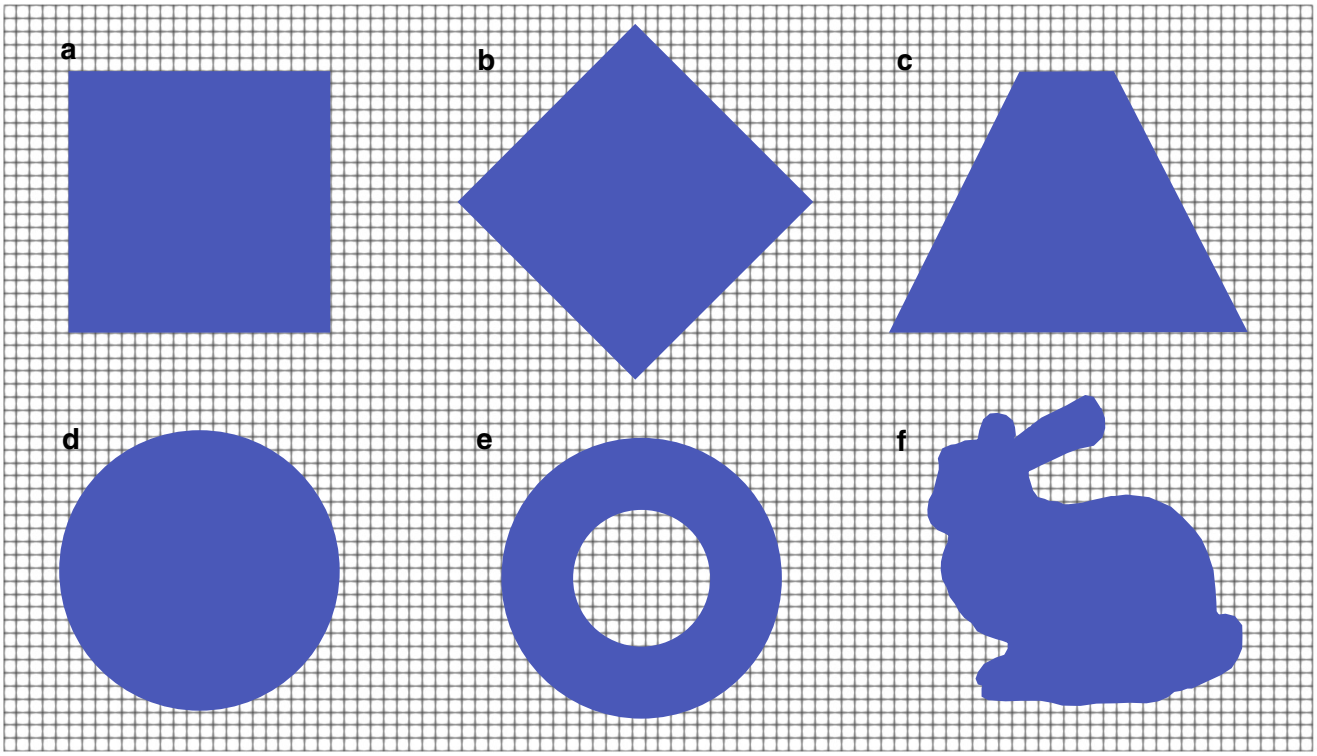

FIGURE 1 | Illustration of material domains with varying geometries embedded in a regular background mesh. Except for the square domain in (a), all other geometries are partially or fully nonconforming with respect to the grid.

flux method (VHFM), including the underlying concept, the modified strong and weak formulations of the governing equations, and the corresponding solution algorithm. The accuracy and convergence properties of the proposed method are systematically verified through a series of benchmark problems in Section 4. Finally, concluding remarks and perspectives for future work are provided in Section 5.

2 | MPM for Heat Transfer Problem

In this section, we present the fundamental MPM framework for heat transfer analysis, including the governing equations, thermal boundary conditions, and their discretizations within the MPM formulation. We begin by introducing the mathematical notation adopted throughout this work. The symbol $\dot{\square}$ denotes the first-order material time derivative. The operators $\square \cdot \square$ and $\square : \square$ represent the single and double tensor contractions, respectively, while $\square \otimes \square$ denotes the tensor product. Additionally, the subscripts $\square_p$ and $\square_I$ denote quantities associated with material points (also referred to as particles, indexed by p) and background grid nodes (indexed by I), respectively. Throughout this study, bold or blackboard bold notation is used to denote spatial variables in tensorial form.

2.1 | Heat Transfer Equation

We consider transient heat transfer governed solely by thermal conduction within a material domain $\Omega \subset \mathbb{R}^d$ ($d = 2$ or 3) (with boundary $\partial\Omega$) over the time interval $\mathcal{T} = [0, t]$. In the absence of mechanical work and phase change, the local energy balance is expressed as [6, 34],

$$\rho c\, \dot{T} + \nabla \cdot \boldsymbol{q} = Q \quad \text{in } \Omega \times \mathcal{T}, \tag{1}$$

where T is the temperature, ρ is the material density, c is the specific heat capacity, $\boldsymbol{q}$ is the conductive heat flux vector ($W \cdot m^{-2}$), and Q denotes the volumetric heat source ($W \cdot m^{-3}$).

Heat conduction is assumed to follow Fourier's law,

$$\boldsymbol{q} = -\boldsymbol{\kappa} \nabla T, \tag{2}$$

where $\boldsymbol{\kappa}$ is the thermal conductivity. In this study, heat transfer is assumed to be isotropic, and therefore $\boldsymbol{\kappa}$ is reduced to a scalar constant κ.

The boundary $\partial\Omega$ is decomposed into two nonoverlapping parts, $\partial\Omega_T$ and $\partial\Omega_q$, on which temperature (Dirichlet) and heat flux (Neumann) boundary conditions are prescribed, respectively. The thermal boundary conditions are defined as

$$T = \hat{T} \qquad \text{on } \partial\Omega_T \times \mathcal{T}, \tag{3}$$

$$-\boldsymbol{q} \cdot \boldsymbol{n} = \hat{q} \qquad \text{on } \partial\Omega_q \times \mathcal{T}, \tag{4}$$

$$-\boldsymbol{q} \cdot \boldsymbol{n} = \gamma(T - T_a) \quad \text{on } \partial\Omega_q \times \mathcal{T}. \tag{5}$$

Here, $\hat{T}$ denotes the prescribed temperature on $\partial\Omega_T$, $\hat{q}$ is the prescribed inward heat flux on $\partial\Omega_q$, and $\boldsymbol{n}$ is the outward unit normal vector to the boundary. Equation (4) represents a conductive heat flux boundary condition, while Equation (5) describes convective heat exchange between the material surface and the surrounding environment, where γ is the convective heat-transfer coefficient and T_a is the ambient temperature. The convective boundary condition describes surface heat exchange processes commonly encountered in natural and engineering systems, such as heat transfer between the ground surface and the atmosphere, or between solid structures and surrounding fluids.

2.2 | Weak Form and MPM Discretization

Let δT denote an admissible virtual temperature field that satisfies the essential (Dirichlet) boundary conditions. Multiplying the heat transfer equation by δT, integrating over the domain Ω, and applying integration by parts together with the divergence theorem, the weak form of the heat conduction equation is obtained as,

$$\int_\Omega \rho c\, \dot{T}\, \delta T\, dV = \int_\Omega \boldsymbol{q} \cdot \nabla \delta T\, dV - \int_{\partial\Omega_q} \hat{q}\, \delta T\, dS + \int_\Omega Q\, \delta T\, dV, \tag{6}$$

where $\nabla\delta T$ denotes the gradient of the virtual temperature field.

In the MPM, the material domain is discretized by n_p material points (particles), each carrying mass, volume, and state variables, and the volume integral is approximated by a summation over particles as follows:

$$\int_\Omega (\cdot) dV = \sum_{p=1}^{n_p} (\cdot) V_p, \tag{7}$$

where V_p is the particle volume. Therefore, the weak form Equation (6) can be discretized into a summation form,

$$\sum_{p=1}^{n_p} V_p \rho_p c_p \dot{T}_p\, \delta T_p = \sum_{p=1}^{n_p} V_p \boldsymbol{q}_p \cdot \nabla \delta T_p + \sum_{p=1}^{n_p} V_p Q_p\, \delta T_p - \int_{\partial\Omega_q} \hat{q}\, \delta T\, dS, \tag{8}$$

where ρ_p, c_p, T_p, $\boldsymbol{q}_p$, and Q_p denote the particle density, heat capacity, temperature, conductive heat flux, and volumetric heat source, respectively. If no prescribed heat flux is applied on the boundary (i.e., $\hat{q} = 0$), the boundary integral vanishes.

The particle temperature T_p and its virtual counterpart δT_p are interpolated from the background grid nodal values using MPM shape functions S_{Ip} as

$$T_p = \sum_{I=1}^{n_n} S_{Ip} T_I, \qquad \delta T_p = \sum_{I=1}^{n_n} S_{Ip} \delta T_I, \tag{9}$$

where T_I and δT_I are the nodal temperature and virtual temperature at node I, and n_n is the number of grid nodes.

Substituting Equation (9) into Equation (8) and exploiting the arbitrariness of δT_I leads to the semi-discrete nodal temperature equation:

$$C_I\, \dot{T}_I = \mathcal{E}_I^{\text{int}} + \mathcal{E}_I^{\text{ext}}, \tag{10}$$

where the nodal heat capacity, internal heat contribution, and external heat contribution are defined as

$$C_I = \sum_{p=1}^{n_p} V_p \rho_p c_p S_{Ip}, \tag{11}$$

$$\mathcal{E}_I^{\text{int}} = \sum_{p=1}^{n_p} V_p \boldsymbol{q}_p \cdot \nabla S_{Ip}, \tag{12}$$

$$\mathcal{E}_I^{\text{ext}} = \sum_{p=1}^{n_p} V_p Q_p S_{Ip} - \int_{\partial\Omega_q} \hat{q}\ S_I\ dS. \tag{13}$$

In Equation (12), the conductive heat flux at each particle is evaluated from the interpolated temperature gradient according to Fourier's law:

$$\boldsymbol{q}_p = -\kappa \nabla T_p = -\kappa \sum_{I=1}^{n_n} T_I \nabla S_{Ip}. \tag{14}$$

The explicit forward Euler integration scheme adopted for the temporal discretization of the transient heat equation is conditionally stable. To prevent numerical oscillations and ensure a converged solution, the time step Δt must be constrained by the critical time step Δt_{cr}, derived from the CourantFriedrichsLewy (CFL) condition adapted for diffusion problems:

$$\Delta t \leq \Delta t_{\text{cr}} = \frac{h_{\text{min}}^2}{\alpha}, \tag{15}$$

where h_{min} denotes the minimum mesh size and $\alpha = k/(\rho c)$ is the thermal diffusivity.

2.3 | Conventional Heat Flux Boundary Imposition

As indicated by the weak form in Equation (6), the enforcement of heat flux boundary conditions requires the evaluation of a surface integral over the Neumann boundary $\partial\Omega_q$. In the FEM, this operation is straightforward because mesh nodes and element faces are explicitly aligned with the material boundary, allowing direct numerical integration using boundary elements. In the MPM, however, as aforementioned, the background grid usually does not conform to the evolving material boundary. A commonly adopted strategy to impose heat flux boundary conditions in MPM is the use of *boundary particles*. These particles constitute a subset of material points that are identified as being located in the vicinity of the boundary $\partial\Omega_q$. The prescribed heat flux is applied to these boundary particles, and the resulting thermal contribution is converted into nodal quantities.

Under this approach, the boundary integral of the prescribed heat flux is approximated as

$$\int_{\partial\Omega_q} \hat{q} S_I\ dS \approx \sum_{p=1}^{n_p} A_p \hat{q}_p S_{Ip} = \sum_{p=1}^{n_p} V_p h_p^{-1} \hat{q}_p S_{Ip}, \tag{16}$$

where A_p denotes the effective surface area associated with a boundary particle, V_p is the particle volume, and h_p represents an assumed characteristic thickness of the boundary particle normal to the surface. Despite its conceptual simplicity, this conventional boundary particle-based approach suffers from several inherent limitations. First, the definition of the particle surface area A_p and the associated thickness h_p is ambiguous, particularly for irregular geometries or curved boundaries. Second, the identification of boundary particles is heuristic and mesh-dependent, which may lead to inconsistent boundary representation as the material undergoes large deformation or particle redistribution.

Alternatively, heat flux boundary conditions may be imposed directly at the grid-nodal level without introducing boundary particles. In this nodal-based approach, the surface integral of the prescribed heat flux is approximated as

$$\int_{\partial\Omega_q} \hat{q} S_I\ dS \approx \sum_{I=1}^{n_I} A_I \hat{q}_I S_I, \tag{17}$$

where A_I denotes the effective boundary surface area associated with node I, and $\hat{q}_I$ is the prescribed heat flux applied at that node. This approach requires the explicit identification of boundary nodes and the assignment of appropriate nodal

surface areas. Similarly, as the background grid in MPM does not conform to the material boundary, the determination of A_I is nonunique and generally mesh-dependent.

These drawbacks of conventional heat flux boundary imposition methods motivate the development of alternative boundary-treatment strategies that avoid explicit surface reconstruction and provide a more robust and accurate enforcement of heat flux boundary conditions within the MPM framework.

3 | Virtual Heat Flux Method (VHFM)

The VHFM is proposed to impose heat flux boundary conditions in the MPM without explicit boundary reconstruction, boundary particles, or nodal surface integration. The key idea is to replace the surface heat flux contribution with an equivalent volumetric contribution defined on an auxiliary *virtual domain*.

3.1 | Virtual Domain and Virtual Heat Flux

We introduce an auxiliary *virtual domain* $\overline{\Omega}$ such that its intersection with the physical domain Ω coincides with the material boundary,

$$\overline{\Omega} \cap \Omega = \partial\Omega. \tag{18}$$

The virtual domain may be chosen as an arbitrary layer that surrounds the material boundary, as illustrated in Figure 2. It does not represent a physical region of the body, but rather serves as a mathematical construct that enables the reformulation of surface boundary contributions into equivalent volumetric terms.

Within $\overline{\Omega}$, a virtual heat flux field $\overline{\boldsymbol{q}}$ is defined to satisfy the prescribed heat flux boundary condition,

$$\overline{\boldsymbol{q}} \cdot \boldsymbol{n} = \begin{cases} \hat{q}, & \text{on } \partial\Omega_q, \\ 0, & \text{on } \partial\Omega \setminus \partial\Omega_q, \end{cases} \tag{19}$$

This construction ensures that the prescribed heat flux is enforced exactly in the normal direction, while naturally vanishing on boundaries where no flux is applied.

In addition, the virtual heat flux field is required to satisfy a homogeneous heat-transfer equation within the virtual domain,

$$\rho c\, \dot{\overline{T}} + \nabla \cdot \overline{\boldsymbol{q}} = 0 \quad \text{in } \overline{\Omega}, \tag{20}$$

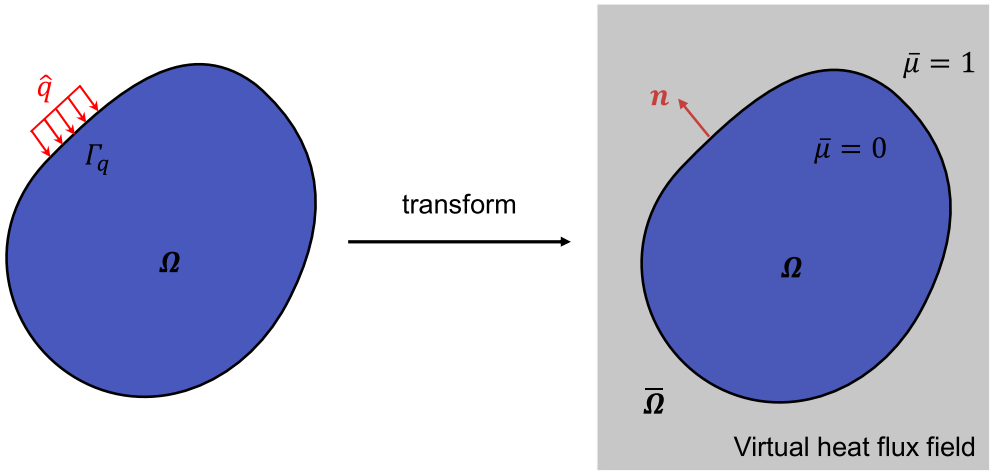

FIGURE 2 | Schematic illustration of the virtual domain $\overline{\Omega}$ surrounding the physical domain Ω and the associated virtual heat flux field.

where $\overline{T}$ is an auxiliary temperature field defined solely for theoretical consistency. Importantly, $\overline{T}$ is not a physical temperature and does not need to be solved explicitly. Its sole purpose is to ensure that the virtual heat flux field admits a divergence form compatible with the governing equation, thereby allowing the boundary heat flux contribution to be incorporated into the weak form as a volumetric term.

Conceptually, the virtual domain and its associated fields act as a mathematical device that "absorbs" the boundary heat flux and redistributes it into the interior weak form. As a result, the original surface integral associated with the Neumann boundary condition is replaced by an equivalent volume integral involving $\overline{\boldsymbol{q}}$, which can be evaluated robustly using standard MPM particle integration. This transformation is the central idea underlying the VHFM.

3.2 | Modified Governing Equation and MPM Discretization

To distinguish quantities defined in the physical and virtual domains, we introduce an indicator function $\overline{\mu}$,

$$\overline{\mu} = \begin{cases} 1, & \text{in } \overline{\Omega}, \\ 0, & \text{in } \Omega. \end{cases} \tag{21}$$

Using this indicator, the governing equations in the physical and virtual domains may be expressed in a unified form over the extended domain $\Omega \cup \overline{\Omega}$ as

$$(1-\overline{\mu})(\rho c\dot{T} + \nabla\cdot\boldsymbol{q} - Q) + \overline{\mu}(\rho c\dot{\overline{T}} + \nabla\cdot\overline{\boldsymbol{q}}) = 0. \tag{22}$$

This combined expression serves only as an intermediate mathematical device that allows the boundary contribution to be embedded into a volumetric formulation.

Invoking the homogeneous governing equation in the virtual domain, Equation (20), and restricting the resulting expression to the physical domain Ω, one obtains

$$\rho c(\dot{T} - \dot{\overline{T}}) + \nabla\cdot(\boldsymbol{q} - \overline{\boldsymbol{q}}) - Q = 0 \quad \text{in } \Omega. \tag{23}$$

Since the auxiliary temperature field $\overline{T}$ is defined only to ensure variational consistency and is not solved explicitly, the difference $(\dot{T} - \dot{\overline{T}})$ may be interpreted as an effective temperature rate that accounts for the presence of the prescribed heat flux boundary condition.

For explicit time integration, this effective rate is approximated by the forward temperature rate at the next time step, yielding the modified strong form

$$\rho c\dot{T}^{k+1} + \nabla\cdot\left(\boldsymbol{q}^{k} - \overline{\boldsymbol{q}}^{k+1}\right) - Q = 0 \quad \text{in } \Omega. \tag{24}$$

This expression differs from the classical heat equation only through the additional divergence term associated with the virtual heat flux, which encapsulates the Neumann boundary condition.

The weak form is obtained by multiplying Equation (24) by an admissible virtual temperature δT and integrating over the physical domain,

$$\int_\Omega \rho c\ \delta T\ \dot{T}^{k+1}\ dV - \int_\Omega \left(\boldsymbol{q}^{k} - \overline{\boldsymbol{q}}^{k+1}\right)\cdot\nabla\delta T\ dV - \int_\Omega \delta T\ Q\ dV = 0. \tag{25}$$

Compared to the conventional weak form, the boundary integral associated with the prescribed heat flux does not appear explicitly. Its effect is instead incorporated through the volumetric term involving $\overline{\boldsymbol{q}}$, which arises naturally from the divergence theorem.

Applying standard MPM discretization, the temperature field and test function are approximated using nodal shape functions. Substitution into Equation (25) leads to the semi-discrete nodal temperature equation

$$\mathcal{C}_{IJ}\dot{T}_J = \widetilde{\mathcal{E}}_I^{\text{int}} + \widetilde{\mathcal{E}}_I^{\text{ext}}, \tag{26}$$

where C_{IJ} is the consistent nodal heat-capacity matrix. The internal and external thermal force vectors are given by

$$\widetilde{\mathcal{E}}_I^{\text{int}} = \sum_{p=1}^{n_p} V_p \, \boldsymbol{q}_p \cdot \nabla S_{Ip} - \sum_{p=1}^{n_p} V_p \, \overline{\boldsymbol{q}}_p \cdot \nabla S_{Ip}, \tag{27}$$

$$\widetilde{\mathcal{E}}_I^{\text{ext}} = \sum_{p=1}^{n_p} V_p \, Q_p \, S_{Ip}. \tag{28}$$

Notably, the conventional surface integral over the Neumann boundary $\partial\Omega_q$ is completely eliminated. The prescribed heat flux is enforced instead through the volumetric contribution associated with the virtual heat-flux field. This reformulation yields a boundary treatment that is fully compatible with the particle integration framework of MPM, avoids explicit surface discretization, and remains robust under large deformations and evolving boundaries.

3.3 | Choice of Virtual Heat Flux Field

Any virtual heat flux field that satisfies Equation (19) may, in principle, be adopted. The virtual field is not unique, and different choices may be constructed provided that the prescribed normal flux on the boundary is recovered. In this work, a particularly simple and robust choice is employed,

$$\overline{\boldsymbol{q}} = \hat{q} \, \boldsymbol{n}. \tag{29}$$

where $\boldsymbol{n}$ is the outward unit normal vector of the physical domain Ω.

This choice possesses several desirable properties. First, it satisfies the prescribed heat flux boundary condition exactly,

$$\overline{\boldsymbol{q}} \cdot \boldsymbol{n} = \hat{q} \, \boldsymbol{n} \cdot \boldsymbol{n} = \hat{q}. \tag{30}$$

Second, the virtual heat flux is purely normal to the boundary, ensuring that no spurious tangential flux components are introduced. Third, the definition of $\overline{\boldsymbol{q}}$ requires only the outward unit normal vector, making it straightforward to implement.

Remark 1. It is emphasized that the virtual heat flux field is not intended to represent the physical heat flux within the body. Instead, it acts as an auxiliary field whose divergence generates an equivalent volumetric contribution in the weak form, replacing the original surface heat flux integral. This nonuniqueness provides flexibility, but the present choice is preferred due to its minimal complexity and consistent performance.

Remark 2. The VHFM formulation is not limited to thermal problems but can be applied directly to general Neumann-type boundary conditions in MPM. Depending on the nature of the prescribed boundary quantity, the corresponding virtual field may be constructed as follows:

3.3.1 | Scalar Neumann Boundary Conditions

For a prescribed scalar flux $\hat{j}$ (e.g., heat flux or fluid flux),

$$\boldsymbol{J} \cdot \boldsymbol{n} = \hat{j} \quad \text{on } \partial\Omega_N, \tag{31}$$

a virtual vector field may be defined as

$$\overline{\boldsymbol{J}} = \hat{j} \, \boldsymbol{n}, \tag{32}$$

which guarantees $\overline{\boldsymbol{J}} \cdot \boldsymbol{n} = \hat{j}$.

3.3.2 | Vector Neumann Boundary Conditions

For a prescribed vector boundary traction $\hat{\boldsymbol{t}}$,

$$\boldsymbol{\sigma} \cdot \boldsymbol{n} = \hat{\boldsymbol{t}} \quad \text{on } \partial\Omega_t, \tag{33}$$

a corresponding second-order virtual stress tensor may be introduced as

$$\overline{\boldsymbol{\sigma}} = \hat{\boldsymbol{t}} \otimes \boldsymbol{n}, \tag{34}$$

which satisfies

$$\overline{\boldsymbol{\sigma}} \cdot \boldsymbol{n} = (\hat{\boldsymbol{t}} \otimes \boldsymbol{n}) \cdot \boldsymbol{n} = \hat{\boldsymbol{t}}. \tag{35}$$

3.3.3 | Tensor Neumann Boundary Conditions

More generally, for higher-order or tensor-valued Neumann boundary conditions, a virtual field of an appropriate order may be constructed by taking the tensor product of the prescribed boundary quantity with the outward normal vector. This construction ensures that the contraction of the virtual field with the normal vector recovers the prescribed boundary condition exactly.

These constructions highlight that VHFM provides a unified and systematic framework for imposing Neumann boundary conditions of different tensorial orders, while maintaining a purely volumetric weak formulation.

3.4 | Surface-Normal Estimation via a Scalar Field

The surface normal can be evaluated using the mass-gradient method, which is simple and widely adopted in the MPM [35, 36]. The nodal mass field exhibits a sharp variation near the material boundary, and its gradient provides a natural approximation of the outward normal direction. This approach avoids additional boundary reconstruction and fits naturally within the standard MPM formulation. For isotropic materials, the outward unit normal at particle p is calculated as

$$\boldsymbol{n}_p = \frac{\nabla m_p}{\|\nabla m_p\|}, \tag{36}$$

with

$$\nabla m_p = \sum_{I=1}^{n_I} m_I \nabla S_{Ip}, \tag{37}$$

where m_I is the nodal mass and S_{Ip} denotes the MPM shape function. However, the mass gradient method may lose accuracy when the material density is inhomogeneous.

Alternatively, the outward unit normal vector required can be evaluated by introducing a *unified scalar field* ϕ that takes a constant value (e.g., $\phi = 1$) for all material points inside the physical domain Ω and is zero outside. The gradient of this field naturally points in the direction of the steepest ascent of the indicator function, which coincides with the outward normal direction at the boundary.

The nodal values of the scalar field are obtained through the standard MPM mapping,

$$\phi_I = \sum_p S_{Ip}\, \phi_p\, V_p, \tag{38}$$

where $\phi_p = 1$ for all material points. The gradient at a material point is then computed as,

$$\nabla \phi_p = \sum_I \phi_I\, \nabla S_{Ip}. \tag{39}$$

Finally, the unit outward normal is given by

$$\boldsymbol{n}_p = \frac{\nabla \phi_p}{\|\nabla \phi_p\|}. \tag{40}$$

This *constant-scalar-gradient method* decouples the normal estimation from the material's density distribution. It is therefore robust in problems involving large density contrasts, nonuniform mass distributions, or purely geometric models where mass is not defined.

Remark 3. Although the mass gradient method is effective in most scenarios, it should be noted that when surface particles become very sparse, the mass gradient may fail to compute an accurate surface normal. In most cases, this issue can be effectively mitigated by increasing the number of particles per cell. Alternatively, more robust surface normal construction approaches, such as the level set method [37], can be further incorporated into the current framework to improve the accuracy of surface detection and normal vector construction. Given the limited scope of this work, these methods are left for future investigation.

3.5 | Solution Algorithms

The numerical implementation of the VHFM is given below and summarized in Algorithm 1.

1. *Boundary node detection*. Boundary nodes are identified via the volume fraction method. If the total particle volume in the cell (denoted as $V_{p\in c}$) relative to the cell volume (denoted as V_c) falls below a prescribed threshold $\eta \in (0,1)$, all nodes for the cell are classified as free surface nodes (node set $\mathcal{N}_1$ in Figure 3). By default, η is taken as 0.5. The corresponding particles associated with these boundary nodes are subsequently assigned as boundary particles (particle set $\mathcal{P}_2$ in Figure 3). Other free surface detection methods can also be adopted [27].
2. *Computation of boundary particle outward unit normal vector*. The unit outward normal vector at each boundary particle is computed using the mass gradient method. The particle mass gradient is evaluated through the summation of nodal mass contributions weighted by the shape function gradients, followed by normalization to obtain the unit normal (Equation (36)).
3. *Imposition of heat-flux boundary conditions*. After identifying the free-surface nodes and computing the corresponding particle outward normals, the prescribed heat-flux boundary condition is enforced in weak form using the virtual

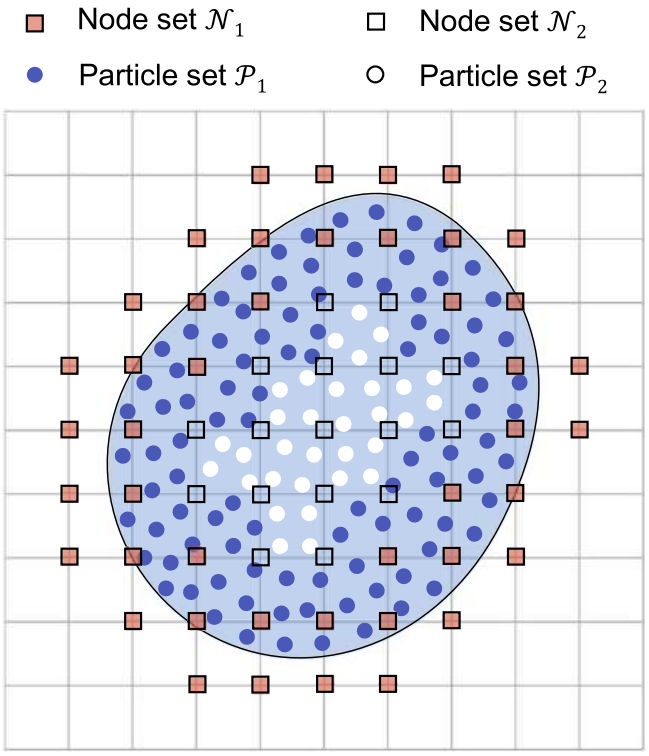

FIGURE 3 | Conceptual illustration of surface nodes and surface particles. P_1: surface particle set; P_2: non-surface particle set; N_1: surface node set; P_2: non-surface node set.

ALGORITHM 1 | Virtual heat flux method for thermal boundary condition impositions.

Require:

Step 1: Identify free surface nodes
$\mathcal{N}_1 \leftarrow \emptyset$
$N_c \leftarrow$ number of active cells; $V_{p\in cJ} \leftarrow$ total volume of the particles in cell J; $V_J \leftarrow$ volume of the cell J;
for $J = 1$ to N_c **do**
  if $0 < V_{p\in cJ}/V_{cJ} < \eta$ **then** ▷ Volume fraction criterion
    $\mathcal{N}_1 \leftarrow \mathcal{N}_1 \cup \{\text{Nodes} \in J\}$
  end if
end for

Step 2: Compute surface normals via scalar gradient
$n_p \leftarrow$ number of particles
for each node $p = 1$ to n_p **do**
  $n_n \leftarrow$ number of nodes connected to particle p
  for each node $I = 1$ to n_n **do**
    $\phi_I \leftarrow \phi_p S_{Ip}$
  end for
end for
for each particle $p = 1$ to n_p **do**
  Compute scalar gradient: $\nabla\phi_p = \sum_I \phi_I \nabla S_{Ip}$
  Compute unit normal: $\boldsymbol{n}_p = \dfrac{\nabla\phi_p}{\|\nabla\phi_p\|}$
end for

Step 3: Impose boundary flux via VHFM
for each particle $p = 1$ to n_p **do**
  for each node $I = 1$ to n_n **do**
    if $I \in \mathcal{N}_1$ **then**
      $\mathcal{E}_I^{\text{int}} \leftarrow \mathcal{E}_I^{\text{int}} + V_p\, \hat{q}_p\, \boldsymbol{n}_p \cdot \nabla S_{Ip}$
    end if
  end for
end for
return Updated $\mathcal{E}_I^{\text{int}}$

flux formulation. The virtual heat flux defined at boundary particles is mapped to the nodal internal heat exclusively at free-surface nodes.

4 | Numerical Examples

In this section, the performance of the proposed VHFM for heat flux boundary imposition in the MPM is assessed. Five numerical examples have been conducted with different material geometries and heat flux boundaries, each with a specific purpose:

1. First, a 1D semi-infinite rod test with constant and convective flux boundaries is conducted, aiming to verify the fundamental accuracy and spatial convergence of the VHFM by direct comparison with analytical results.
2. Second, the heating of a 2D circular ring (with both concave and convex boundaries) is simulated, aiming to demonstrate the method's capability for handling complex static geometries without boundary conformity, verified against reference finite difference solutions.
3. Third, the convective cooling of a 3D sphere is simulated to demonstrate the method's effectiveness in modeling 3D scenarios. The effect of particles per cell on the accuracy is also investigated.

4. Moreover, the heating of a rotating 2D square block is simulated, involving both fixed-angle and continuously rotating configurations, aiming to validate the method's accuracy and robustness for dynamically evolving nonconforming boundaries under rigid-body motion.
5. Furthermore, the method is applied to a practical problem, the cooling of a rotating fan with complex geometry, aiming to showcase the method's robustness and applicability in simulating heat transfer processes with intricate, moving boundaries.
6. Finally, a thermo-mechanical coupling example including the heating of a collapsing soil column is presented to demonstrate that the proposed method is also applicable to large deformation scenarios, provided that the surface particles are sufficiently dense to enable an accurate construction of the surface normal.

4.1 | 1D example: Transient Heat Transfer in a Semi-Infinite Rod

In the first example, we simulate the transient heat transfer problem of a semi-infinite rod under a heat flux boundary. This problem can be simplified to a one-dimensional (1D) scenario, as illustrated in Figure 4a, where the left boundary is subjected to a heat flux q_s. To approximate a semi-infinite condition, the rod length, L, is set to a sufficiently large size of 20 m, and we focus only on the results within the first 5 m region. The simulation is conducted using a unity material assumption, where all material properties, including the density $\rho\ (kg/m^3)$, the specific heat capacity $c\ (J/(kg{\cdot}°C))$, and the thermal conductivity κ (W/(m·°C)), are set to 1. The initial temperature, T_0, is set to 0°C. We examined both a constant heat flux boundary and a convective heat flux boundary condition. For the former, the applied heat flux q_s is set to 1 W/m^2. For the latter, the ambient temperature, T_a, is set to 1°C, and the convective heat transfer coefficient, γ, is also set to 1 $W/(m^2{\cdot}°C)$.

The analytical solution for the temperature at location x and time t is expressed as follows:

- For constant heat flux boundary:

$$T(x,t) = T_0 + 2\frac{q_s}{\kappa}\sqrt{\frac{\alpha t}{\pi}}\left[\exp\left(\frac{-x^2}{4\alpha t}\right) - \frac{1}{2}x\sqrt{\frac{\pi}{\alpha t}}, \operatorname{erfc}\left(\frac{x}{2\sqrt{\alpha t}}\right)\right], \tag{41}$$

- For convective heat flux boundary:

$$T(x,t) = T_0 + (T_a - T_0)\left[\operatorname{erfc}\left(\frac{x}{2\sqrt{\alpha t}}\right) - \exp\left(\frac{\gamma x}{\kappa} + \frac{\gamma^2 \alpha t}{\kappa^2}\right)\cdot \operatorname{erfc}\left(\frac{x}{2\sqrt{\alpha t}} + \frac{\gamma\sqrt{\alpha t}}{\kappa}\right)\right], \tag{42}$$

where $\alpha = \kappa/(\rho c)$ is the thermal diffusivity and erfc is the complementary error function. The detailed derivation of the above analytical solution is presented in Appendix A.

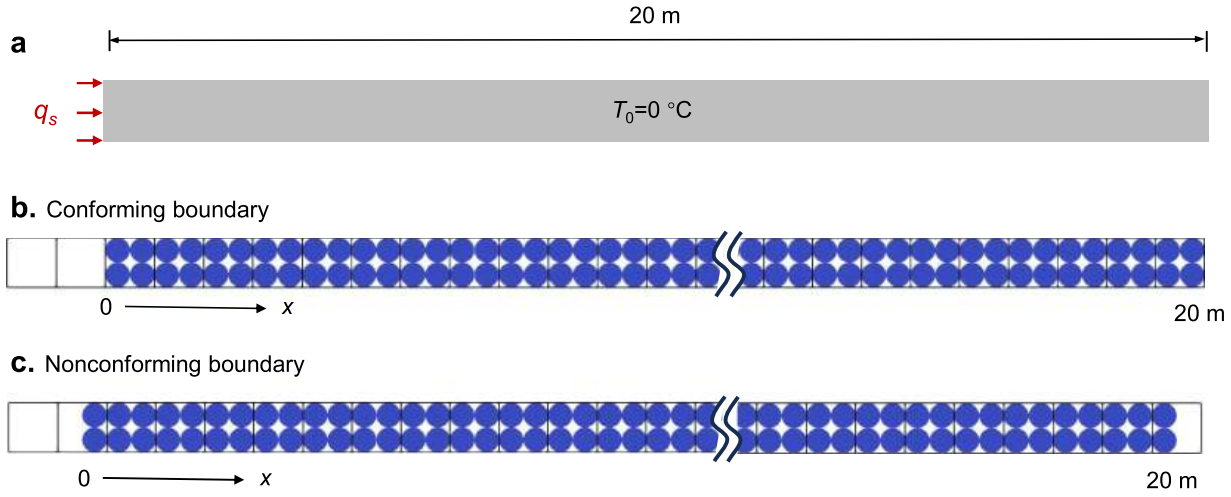

FIGURE 4 | Transient heat transfer in a 1D semi-infinite Rod: (a) model geometry, initial and boundary conditions, (b) conforming boundary configuration, and (c) nonconforming boundary configuration.

A background grid with a cell size of 0.1 m is employed for the simulation. The material point size is set to half of the grid size, that is, 0.05 m. Two different arrangements of material points are considered, as illustrated in Figure 4. In Figure 4b, the material points are arranged in a *conforming boundary* configuration, where each grid cell contains four evenly distributed material points, and the material points at the left boundary align with the grid boundary. In contrast, Figure 4c shows a *nonconforming boundary* configuration, where all material points are shifted leftward by half of a grid size. In this case, the leftmost grid cell contains only two material points. The VHFM is employed to test both the conforming and nonconforming boundary configurations. For comparison, in the conforming boundary configuration, two additional simulations are conducted by applying the boundary conditions either directly at the nodes or at the material points. A uniform time step of $\Delta t = 1 \times 10^{-3}$ s is used for the simulations.

Remark 4. Note that the material points in our simulations are arranged in the commonly used equidistant configuration, located at positions 0.25 h_e and 0.75 h_e within each grid cell, rather than being precisely positioned at the Gaussian integration points. While this arrangement may introduce additional integration errors, these errors are consistent across all cases and therefore do not affect the validity of our conclusions.

Figure 5a,b compare the temperature distributions at time instants $t = 0.1$ s and $t = 0.5$ s, obtained using the MPM with VHFM and the analytical solution. It can be observed that for both constant and convective heat flux boundaries, the temperature fields simulated using VHFM agree very well with the theoretical solution, regardless of whether the boundary is conforming or nonconforming.

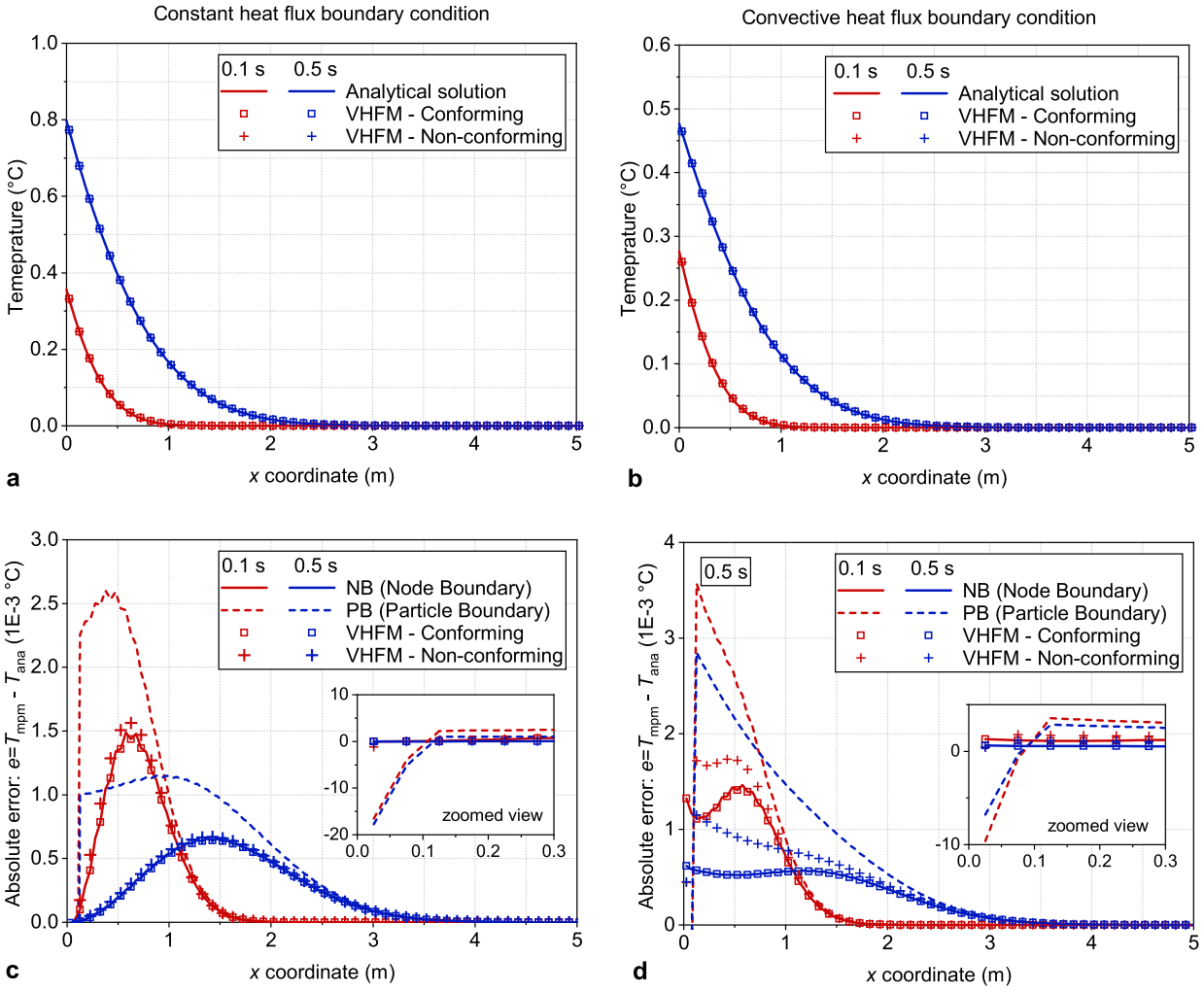

FIGURE 5 | Transient heat transfer in a 1D semi-infinite Rod with both constant heat flux boundary (left column) and convective heat flux boundary (right column): (a-b) comparison of the temperature distributions at time instants of 0.1 s and 0.5 s obtained using MPM with VHFM and the analytical solution; (c-d) comparison of the absolute error for different boundary condition imposition methods. The zoomed-in views in (c) and (d) highlight the error near the origin, i.e., at the heat flux boundary, indicating that applying heat flux directly at the particle boundary results in significant errors near the boundary.

TABLE 1 | Transient heat transfer in a 1D semi-infinite Rod: comparison of RMSE ε_{err} using different boundary condition imposition methods.

Time	Node boundary (NB)	Particle boundary (PB)	VHFM-Conforming	VHFM-nonconforming
Constant heat flux boundary condition				
0.1 s	2.420×10^{-4}	9.714×10^{-4}	2.420×10^{-4}	2.599×10^{-4}
0.5 s	1.608×10^{-4}	9.803×10^{-4}	1.608×10^{-4}	1.661×10^{-4}
1.0 s	1.352×10^{-4}	9.826×10^{-4}	1.352×10^{-4}	1.383×10^{-4}
Convective heat flux boundary condition				
0.1 s	2.810×10^{-4}	7.173×10^{-4}	2.810×10^{-4}	2.065×10^{-4}
0.5 s	1.748×10^{-4}	6.159×10^{-4}	1.748×10^{-4}	2.574×10^{-4}
2.5 s	8.463×10^{-5}	5.756×10^{-4}	8.463×10^{-5}	3.392×10^{-4}

To quantitatively analyze the simulation error, the absolute error, $e_p = T_{\text{mpm, } p} - T_{\text{ana, } p}$, is plotted in Figure 5c,d, where $T_{\text{mpm, } p}$ and $T_{\text{ana, } p}$ represent the simulated and theoretical temperatures at material point p, respectively. Additionally, the root mean square error (RMSE), ε_{err}, between the temperature field obtained from the MPM simulation and the analytical solution is calculated.

$$\varepsilon_{\text{err}} = \sqrt{\frac{1}{N_p}\sum_{p=1}^{N_p}(T_{\text{mpm, } p} - T_{\text{ana, } p})^2}, \tag{43}$$

where N_p is the total number of material points.

Figure 5c,d further compare the absolute errors obtained using the VHFM and the conventional particle and node boundary approaches (both under the conforming condition). Table 1 summarizes the calculated ε_{err} at different time instants for various boundary imposition methods. The results show that for conforming boundaries, the accuracy of the VHFM simulation is identical to that of directly applying the boundary conditions at the nodes, both of which are significantly more accurate than applying the boundary conditions at the particles. For nonconforming boundaries, the accuracy of the VHFM is slightly lower but remains close to that of the conforming condition with node-based boundary imposition, and it is still far more accurate than the particle-based approach. These findings demonstrate that the proposed VHFM achieves excellent accuracy when imposing heat flux boundaries.

To verify the convergence of the method, we further tested the error ε_{err} under different mesh sizes. Five mesh sizes (h_e) were considered: 0.5, 0.2, 0.1, 0.05, and 0.02 m. Since explicit integration is used, the time step must be sufficiently small to ensure stability for each case. As the time step size also influences the magnitude of the error, we fixed the time step for each mesh size at 4×10^{-5} s. In this study, we tested only the nonconforming boundary condition for both the VHFM and the conventional boundary particle method. The calculated errors at different time instants are listed in Table 2. Figure 6 presents the variation of ε_{err} with respect to $1/h_e$ in log-log space. It is evident that the VHFM achieves a quadratic convergence for both constant and convective heat flux boundary conditions. In contrast, the conventional boundary particle method exhibits inferior accuracy and convergence rate compared to the VHFM.

4.2 | 2D example: Heating of a Circular Ring

The second example simulates the heating of a two-dimensional (2D) circular ring, aiming to verify the accuracy of VHFM for curved boundaries. As depicted in Figure 7a, the outer and inner radii of the ring are $R_1 = 5$ m and $R_2 = 1$ m, respectively. A heat flux q_s is applied simultaneously to both the inner and outer boundaries of the circular ring. The initial temperature of the circular ring is set to 0°C. Two types of heat flux boundary conditions are considered: a constant heat flux $q_s = 1$ W/m^2, and a convective heat flux boundary condition $q_s = \gamma(T - T_a)$, with the ambient temperature $T_a = 1$°C and the heat transfer coefficient $\gamma = 1$ W/(m^2·°C). Again, we assume unity material for the ring, i.e., density $\rho = 1$ kg/m^3, specific heat capacity $c = 1$ J/(kg·°C), and thermal conductivity $\kappa = 1$ W/(m·°C).

TABLE 2 | Transient heat transfer in a 1D semi-infinite Rod: errors with mesh refinement using VHFM and particle boundary (PB) for both constant and convective heat flux boundary conditions.

	h_e	0.5 m	0.2 m	0.1 m	0.05 m	0.02 m
Constant heat flux boundary condition						
VHFM	0.1 s	7.011×10^{-3}	1.187×10^{-3}	2.599×10^{-4}	6.015×10^{-5}	9.752×10^{-6}
	0.5 s	5.131×10^{-3}	6.887×10^{-4}	1.661×10^{-4}	4.017×10^{-5}	6.467×10^{-6}
	1.0 s	3.981×10^{-3}	5.669×10^{-4}	1.383×10^{-4}	3.377×10^{-5}	5.428×10^{-6}
PB	0.1 s	9.357×10^{-3}	2.362×10^{-3}	7.240×10^{-4}	2.385×10^{-4}	5.769×10^{-5}
	0.5 s	9.618×10^{-3}	2.018×10^{-3}	6.694×10^{-4}	2.289×10^{-4}	5.670×10^{-5}
	1.0 s	8.795×10^{-3}	1.945×10^{-3}	6.565×10^{-4}	2.266×10^{-4}	5.647×10^{-5}
Convective heat flux boundary condition						
VHFM	0.1 s	4.526×10^{-3}	7.946×10^{-4}	2.065×10^{-4}	5.269×10^{-5}	8.540×10^{-6}
	0.5 s	6.547×10^{-3}	1.043×10^{-3}	2.574×10^{-4}	6.413×10^{-5}	1.024×10^{-5}
	2.5 s	7.242×10^{-3}	1.421×10^{-3}	3.392×10^{-4}	8.017×10^{-5}	1.238×10^{-5}
PB	0.1 s	3.531×10^{-3}	6.853×10^{-4}	2.180×10^{-4}	7.271×10^{-5}	1.772×10^{-5}
	0.5 s	6.828×10^{-3}	1.253×10^{-3}	3.832×10^{-4}	1.254×10^{-4}	3.023×10^{-5}
	2.5 s	8.308×10^{-3}	1.873×10^{-3}	5.570×10^{-4}	1.778×10^{-4}	4.221×10^{-5}

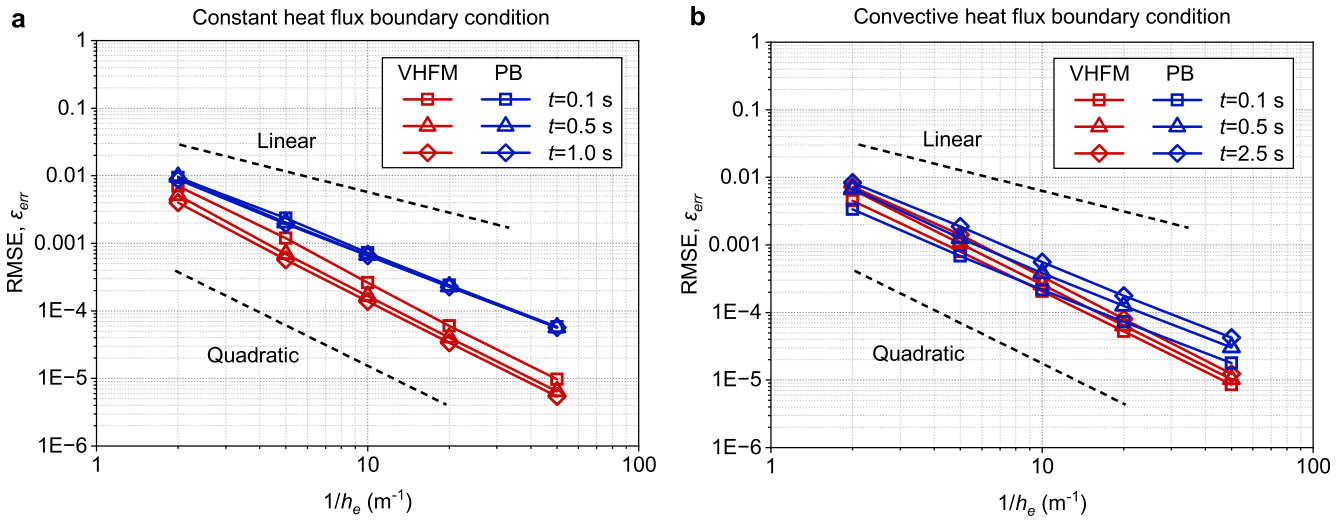

FIGURE 6 | Transient heat transfer in a 1D semi-infinite Rod: Convergence test with mesh refinement for (a) constant heat flux boundary and (b) convective heat flux boundary.

A quadrilateral background grid with a mesh size of 0.1 m is used, and the material point size is set to 0.05 m. To discretize the circular ring, we first generate a 5 m × 5 m square and then remove the material points outside the ring region. The resulting distribution of material points is shown in Figure 7b. It can be observed that the circular ring boundary appears as a staircase pattern and does not align with the background grid. The time step is set to $\Delta t = 1 \times 10^{-3}$ s. The volume fraction threshold is set to 0.55, and the detected surface nodes and surface particles are shown in Figure 7c. Since there is no available analytical solution for this problem, we compare the MPM result with the FDM result. The FDM algorithm adopted for this 2D is shown in Appendix B.

Figure 8 shows the computed surface outward normals for different mesh sizes. Qualitatively, the surface normal results are reasonable, with all normals pointing approximately toward the center of the circle, even on coarse meshes. However, due to the non-smooth boundary, some deviations are inevitable. We further analyzed the error between the theoretical normal vector angle and the computed angle, and calculated the root mean square error (RMSE), as presented in Figure 9.

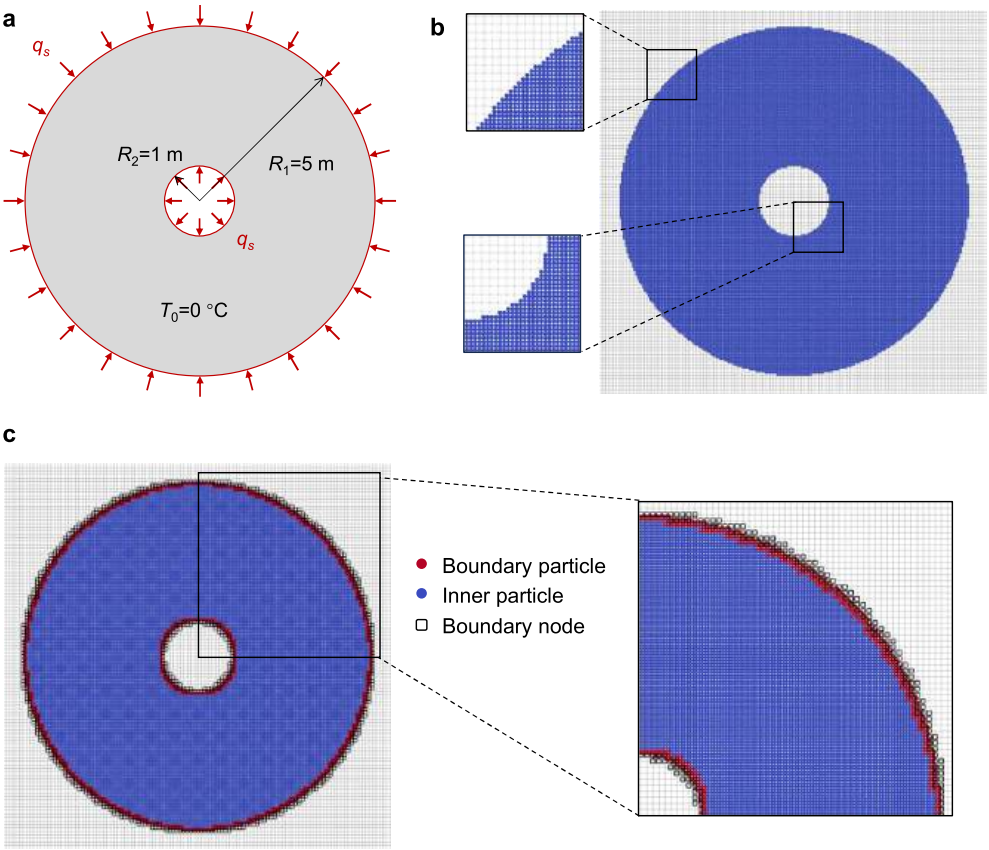

FIGURE 7 | Bidirectional heating of circular ring: (a) model geometry, initial and boundary conditions, (b) background mesh and material point discretizations, and (c) detected surface nodes and surface particles based on the volume fraction method.

It can be observed that most angular errors θ_{err} lie within $\pm 10°$ and exhibit a clearly periodic pattern, which is related to the distribution of boundary particles. The projection error corresponding to 10°, that is, $1 - \cos(\theta_{\text{err}})$, is within 1.15%, indicating that the influence of such error on the overall heat transfer is relatively small. Moreover, the RMSE remains largely independent of mesh size, suggesting that this error is quite controllable. If a more accurate calculation of the surface normal is required, it may be necessary to reconstruct the boundary to make it smoother or to adopt more advanced methods such as the level set method. However, these approaches would introduce additional complexity, which is out of the scope of this work. We will retain the exploration of a more accurate and efficient surface normal construction approach in future work.

Figure 10 presents the simulated temperature distribution at various time instances, along with several temperature contour lines highlighted. As expected, the contour lines remain circular, even in the immediate vicinity of the boundary. Figure 11 quantitatively compares the radial temperature distribution of the ring at $t = 1$ s, obtained from MPM simulations and FDM calculations. For this problem, the FDM solution is based on a 1D axisymmetric model in polar coordinates, using the same mesh size as the MPM (0.1 m). The second-order central difference scheme and three-point one-sided difference for boundary heat flux imposition are employed in the FDM to ensure accuracy. In the MPM simulations, in addition to the 0.1 m grid, two other grid sizes, 0.2 m and 0.05 m, are also tested. The results indicate that the MPM and FDM solutions are in close agreement, and the predictions from MPM with VHFM show minimal variation across different mesh sizes. This demonstrates that even with relatively coarse grids, simulations based on VHFM can still produce reliable results.

Furthermore, Figure 12 compares the temperature evolution at a radial position of 3 m (i.e., along the central axis of the ring). Under the constant heat flux condition, the temperature increases continuously, while under the convective heat flux condition, the temperature gradually approaches the ambient temperature of 1°C. In both cases, the temperature evolution predicted by MPM aligns closely with the FDM results, with simulations across different grid sizes yielding nearly identical results. This further validates the accuracy and robustness of the proposed VHFM in handling nonaligned thermal boundary conditions.

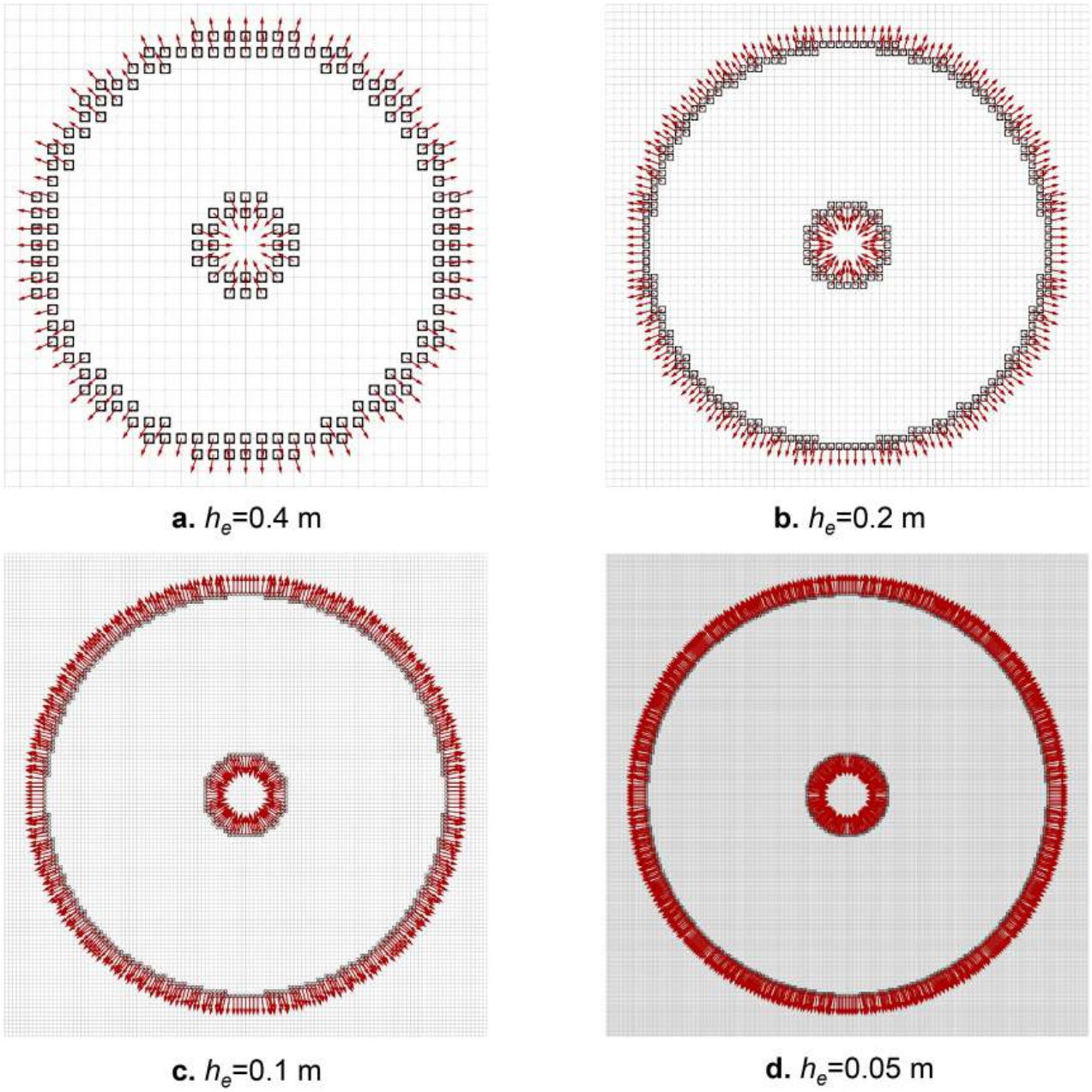

FIGURE 8 | Bidirectional heating of circular ring: surface normal vector for (a) $h_e = 0.4$ m, (b) $h_e = 0.2$ m, (c) $h_e = 0.1$ m, and (d) $h_e = 0.05$ m.

Figure 13a compares the radial heat flux distribution under the constant heat flux condition after reaching steady state ($t = 10$ s) for different mesh sizes. The results show that the heat flux values at the inner and outer boundaries are -1°C/m (directed toward the center) and 1°C/m (directed away from the center), respectively, which are perfectly consistent with the imposed boundary conditions. Even for a coarse mesh ($h_e = 0.2$ m), the differences in the heat flux distribution compared with finer meshes are negligible. Figure 13b,c further present a quantitative comparison of the radial heat flux at $t = 0.1$ s and $t = 10$ s, including results from the FDM and MPM simulations with three different mesh sizes. The results demonstrate that the MPM simulations based on the VHFM are in excellent agreement with the FDM solution, both in the early heating stage ($t = 0.1$ s) and at the final steady state ($t = 10$ s). Moreover, the results across different mesh sizes exhibit good consistency. These findings further validate the accuracy of the proposed VHFM method for thermal boundary imposition.

Finally, a self-convergence test was conducted. Since no analytical solution is available for reference, the simulation results obtained on a 0.025 m grid are treated as the reference solution. The relative errors of the simulation results on grid sizes

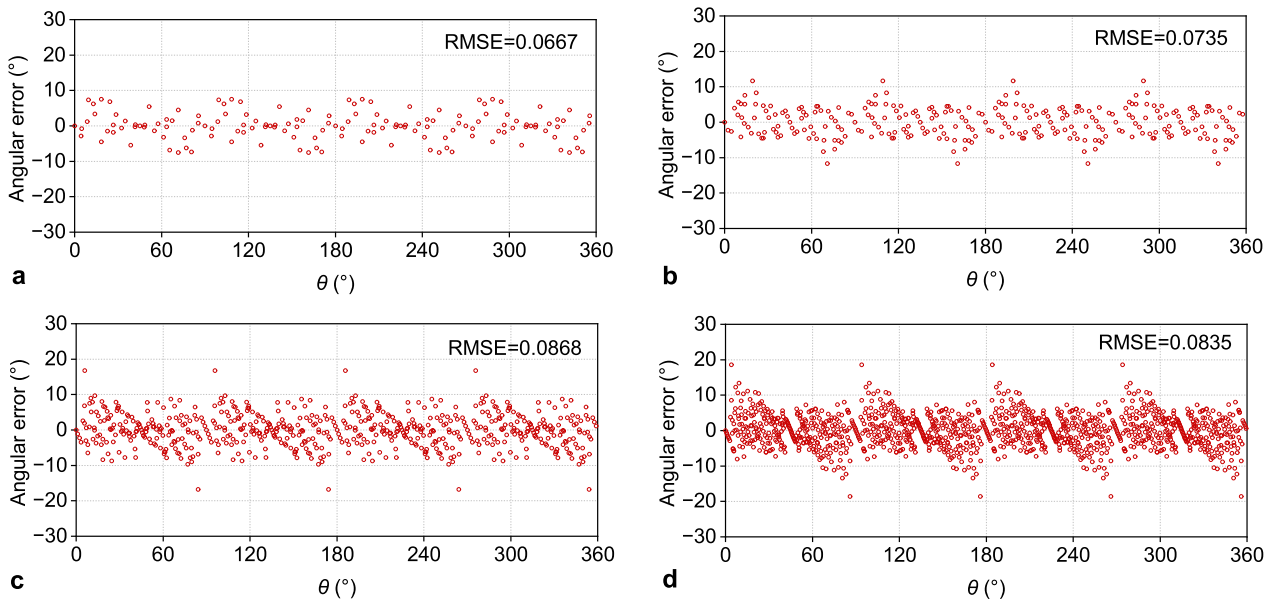

FIGURE 9 | Bidirectional heating of circular ring: error of surface normal (a) $h_e = 0.4$ m, (b) $h_e = 0.2$ m, (c) $h_e = 0.1$ m, and (d) $h_e = 0.05$ m.

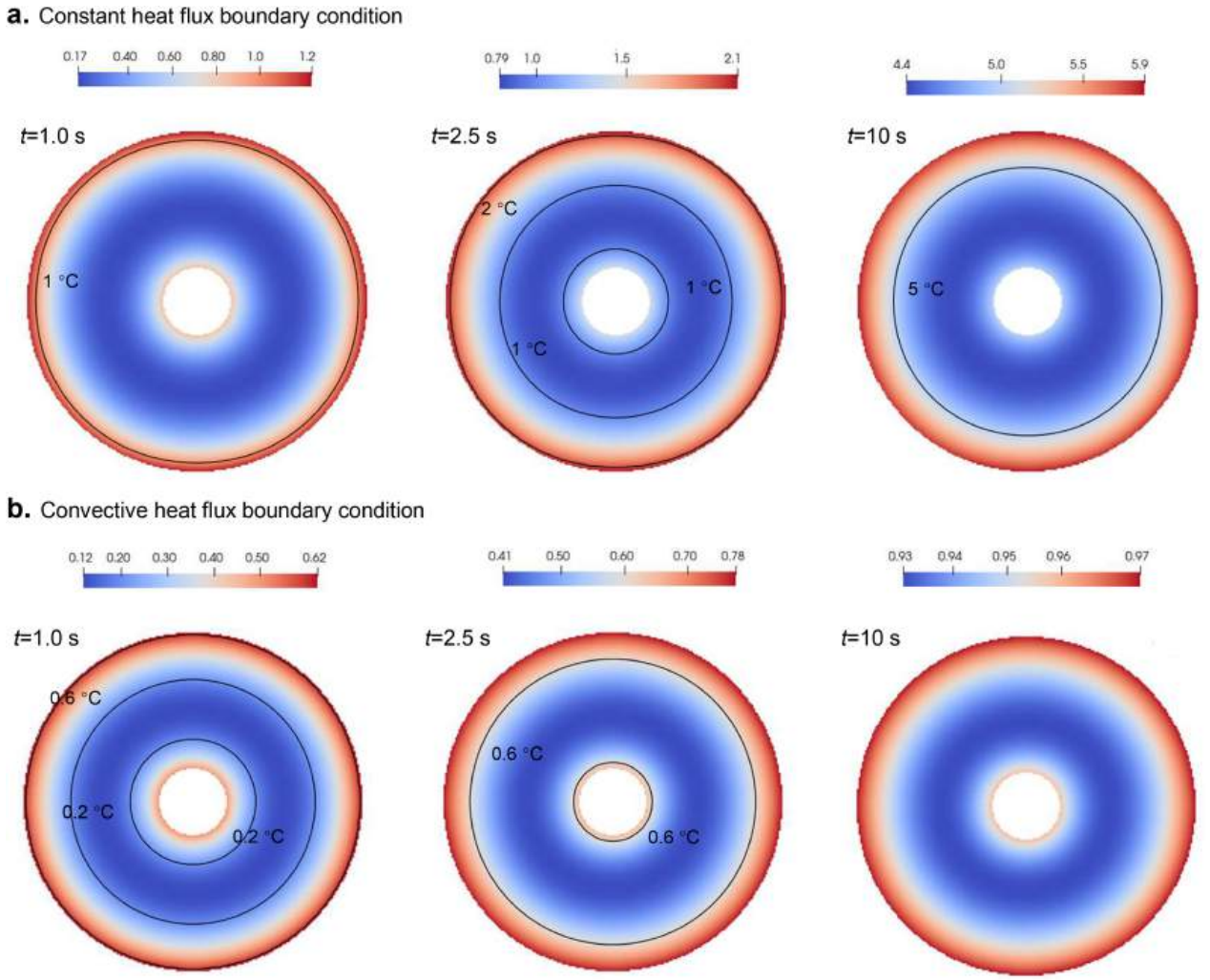

FIGURE 10 | Bidirectional heating of a circular ring: temperature contours for (a) constant heat flux boundary condition and (b) convective heat flux boundary condition at $t = 1.0$, 2.5, and 10 s. The black lines show the isotherms.

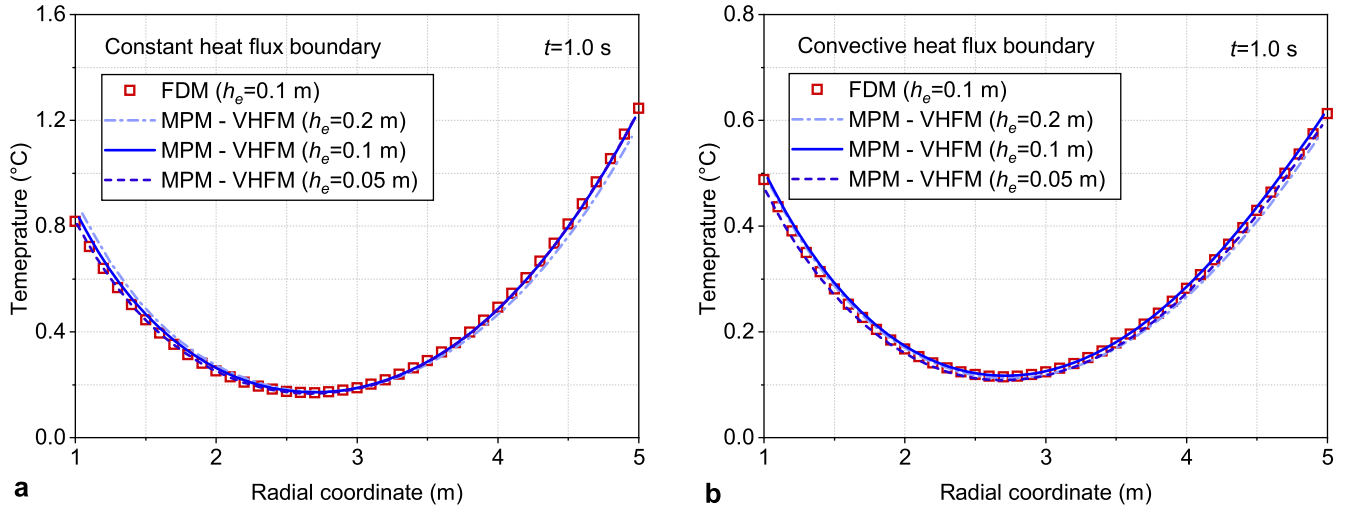

FIGURE 11 | Bidirectional heating of a circular ring: comparison of radial temperature distributions at $t = 1.0$ s obtained using FDM and MPM with VHFM for different mesh sizes, under (a) constant heat flux boundary and (b) convective heat flux boundary.

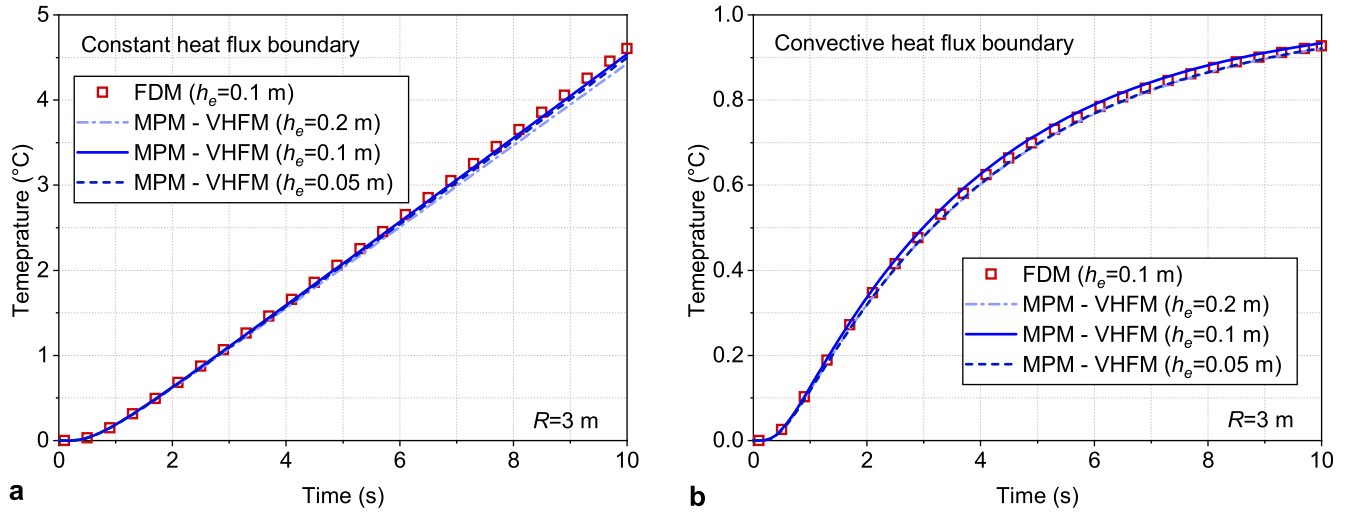

FIGURE 12 | Bidirectional heating of a circular ring: comparison of temperature evolution at a radial distance of $R = 3m$, obtained using FDM and MPM with VHFM for different mesh sizes, under (a) constant heat flux boundary and (b) convective heat flux boundary.

of 0.4, 0.2, 0.1, and 0.05 m are computed as follows:

$$\varepsilon_{\text{err}} = \sqrt{\frac{1}{N_n}\sum_{n=1}^{N_n}(T_n - T_{\text{ref},n})^2}, \tag{44}$$

where T_n and $T_{\text{ref},n}$ denote the nodal temperatures of the test case and the reference case, respectively, and N_n is the total number of active nodes in the test case. It is worth noting that nodal temperatures are used instead of particle temperatures, as this allows an apple-to-apple comparison between nodes in the test and reference meshes, thereby ensuring a fair evaluation.

Table 3 and Figure 14 show the relative errors with respect to $1/h_e$ at three selected time instances. It can be observed that the error decreases gradually with mesh refinement, and the convergence rate lies between linear and quadratic. This convergence rate is lower than the quadratic rate achieved in the 1D test, which can be attributed to the use of a uniform particle discretization to represent the arbitrary boundary in the present study, a factor that may reduce the convergence rate [27].

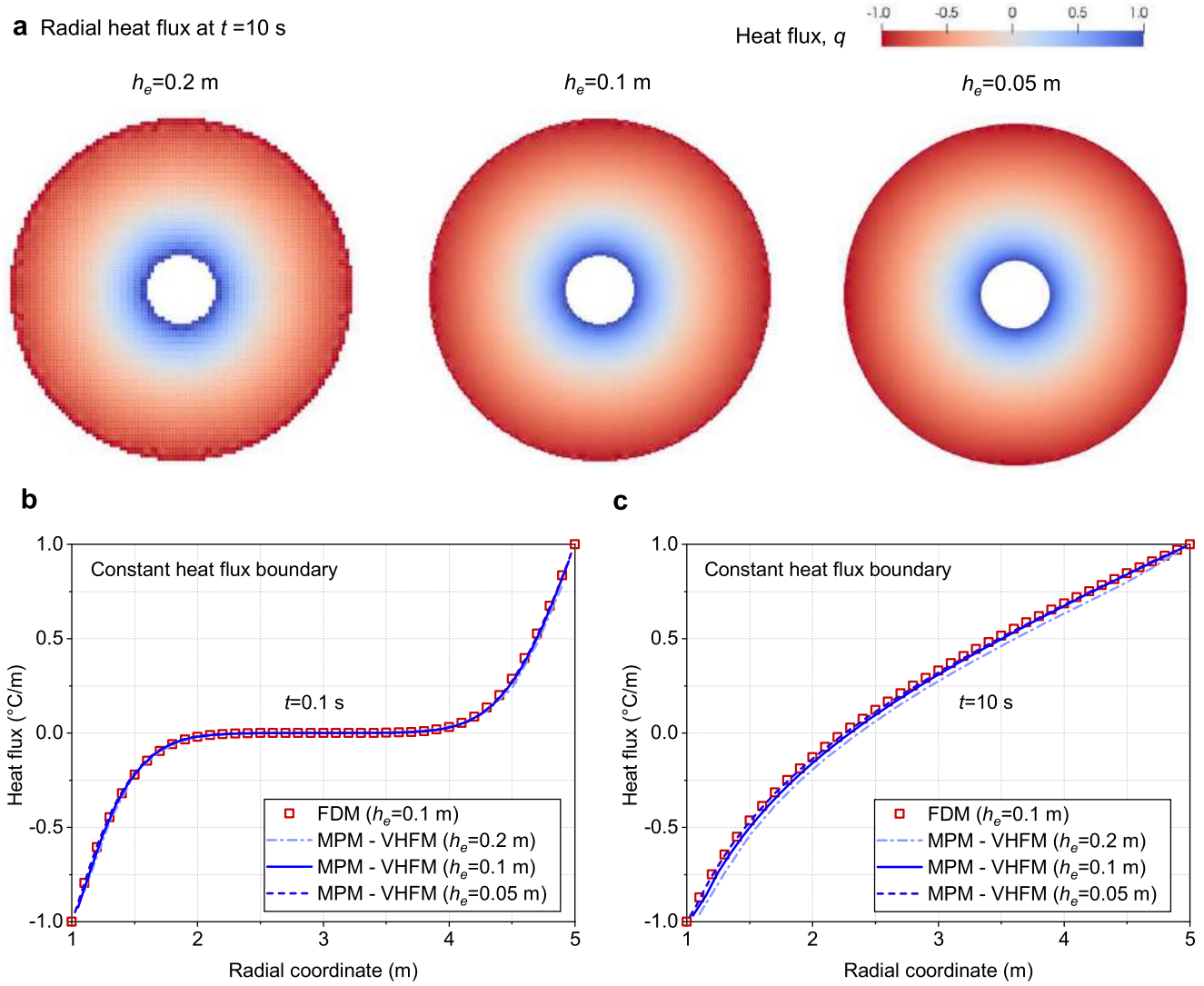

FIGURE 13 | Bidirectional heating of a circular ring under constant heat flux boundary condition: (a) radial heat flux contours with different mesh sizes at $t = 10$ s; (b) heat flux distribution along the radial direction at $t = 0.1$ s; and (c) heat flux distribution along the radial direction at $t = 1.0$ s.

4.3 | 3D Example: Cooling of a Sphere

The third numerical example simulates the transient cooling of a three-dimensional (3D) sphere. The sphere has a radius of 5 m and a uniform initial temperature of 100°C, and it is exposed to an ambient temperature of 0°C with a convective heat transfer coefficient of $\gamma = 1$ W/(m^2·°C). Unit material properties are employed. The simulation utilized a uniform hexahedral background mesh with an element size of 0.2 m (see Figure 15b). Two distinct particle-per-cell (PPC) configurations are examined: 8 particles and 27 particles per background cell. The time step is set to $\Delta t = 1 \times 10^{-2}$ s, and the volume fraction threshold η is consistently maintained at 0.55. Since no available closed-form solution exists for this problem, validation is performed against a finite difference method (FDM) reference solution. The problem can be reduced to 1D heat transfer in spherical coordinates; the specific FDM algorithm is detailed in Appendix C.

Figure 16 illustrates the temperature distribution within the sphere at various time instances, demonstrating the progression of cooling from the surface toward the center. The results for both PPC configurations are visually nearly identical. A quantitative comparison between the MPM predictions and the FDM reference for the radial temperature profile at selected times is presented in Figure 17. The case with PPC = 8 shows good agreement with the FDM results, while the case with PPC = 27 exhibits even closer agreement, confirming that increasing the number of PPC improves numerical accuracy. The FDM solution is considered the more accurate benchmark here, as it solves a simplified 1D problem and

TABLE 3 | Bidirectional heating of a circular ring: relative errors with mesh refinement using VHFM for both constant and convective heat flux boundary conditions.

h_e	0.4 m	0.2 m	0.1 m	0.05 m
Constant heat flux boundary condition				
1 s	7.758×10^{-2}	2.254×10^{-2}	1.289×10^{-2}	5.172×10^{-5}
2.5 s	1.158×10^{-1}	3.541×10^{-2}	1.985×10^{-2}	8.230×10^{-3}
10 s	1.338×10^{-3}	4.071×10^{-4}	3.171×10^{-4}	1.431×10^{-5}
Convective heat flux boundary condition				
1 s	3.087×10^{-2}	8.395×10^{-3}	4.829×10^{-3}	1.706×10^{-3}
2.5 s	2.797×10^{-2}	7.589×10^{-3}	4.830×10^{-3}	1.437×10^{-3}
10 s	6.526×10^{-3}	1.688×10^{-3}	7.123×10^{-4}	2.034×10^{-4}

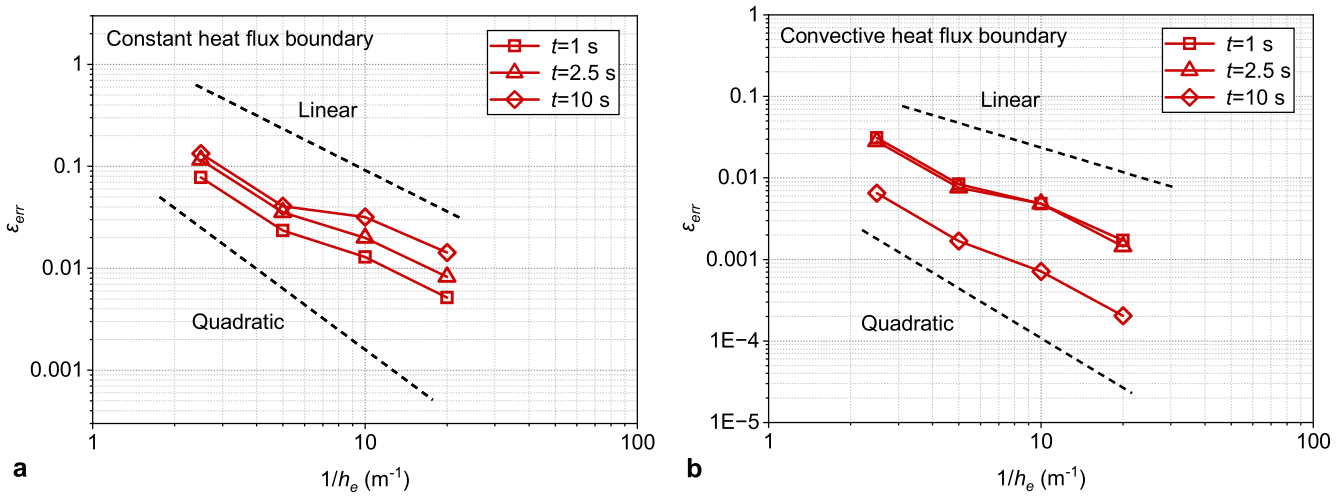

FIGURE 14 | Bidirectional heating of a circular ring: convergence test with mesh refinement for (a) constant heat flux boundary and (b) convective heat flux boundary.

allows for more precise imposition of boundary conditions. However, FDM is generally restricted to problems with simple, regular geometries; for complex shapes, particle-based methods offer superior flexibility. This example demonstrates that the proposed VHFM provides accurate and robust simulations for 3D transient heat transfer problems.

4.4 | Moving Boundary Example: Heating of a Square Block

In the previous example, although the boundary is circular, its geometric configuration remains fixed. To verify that the proposed VHFM can accurately impose thermal boundary conditions under dynamically changing boundary configurations, the third example considers a 2D square domain. The initial boundary of the square is aligned with the grid, after which it is rotated by a certain angle. Convective heat flux boundary conditions are applied simultaneously to all four sides of the square, and only the convective heat flux case is presented here. The model geometry, initial and boundary conditions are depicted in Figure 18a. The side length of the square is 5 m; the initial temperature is 0°C; the ambient temperature is 1°C; and the convective heat transfer coefficient is 1 W/(m^2·°C). The background grid size is 0.2 m, and four material points are assigned within each grid cell. Similar to the previous case, the material properties are set to unit values. The simulation time step size is set to 1×10^{-2} s.

In the MPM simulations, we consider the following two scenarios: (1) fixed rotation angles of 15°, 30°, and 45°; and (2) fixed rotational speeds (denoted by ω) of 1/16, 1/4, 1, and 4 revolutions per second (unit: r/s). The conforming case, where the boundary is aligned with the grid, is used as a reference (Figure 18b). Based on the findings from the first example in Section 4.1, applying boundary conditions using the VHFM produces results equivalent to directly imposing them

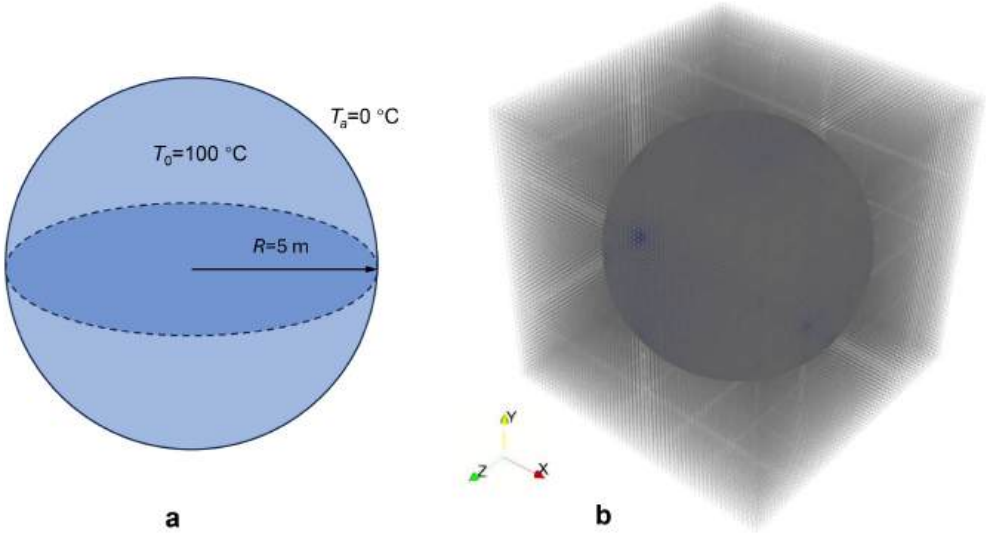

FIGURE 15 | Cooling of a sphere: (a) geometry, initial and boundary conditions; (b) background mesh and material discretization.

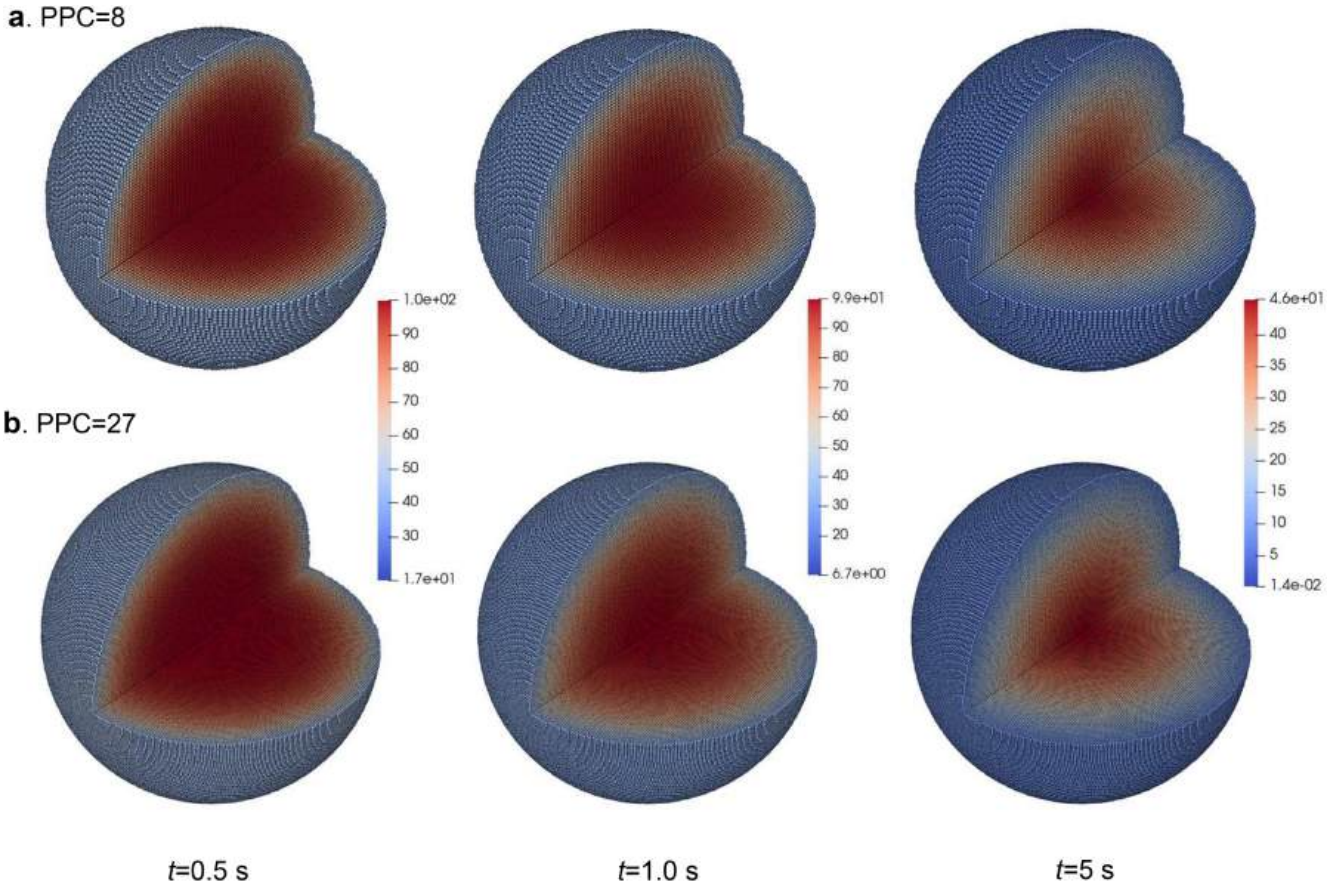

FIGURE 16 | Cooling of a sphere: temperature distribution at various time instants for the case (a) PPC = 8 and (b) PPC = 27.

at the nodes, both of which are more accurate than applying them at the material points. Therefore, VHFM is directly used for boundary condition imposition in the reference case. Since no analytical solution exists for this 2D problem, the FDM results are used as a reference for comparison. Details of the FDM algorithm for this problem can be found in Appendix D.

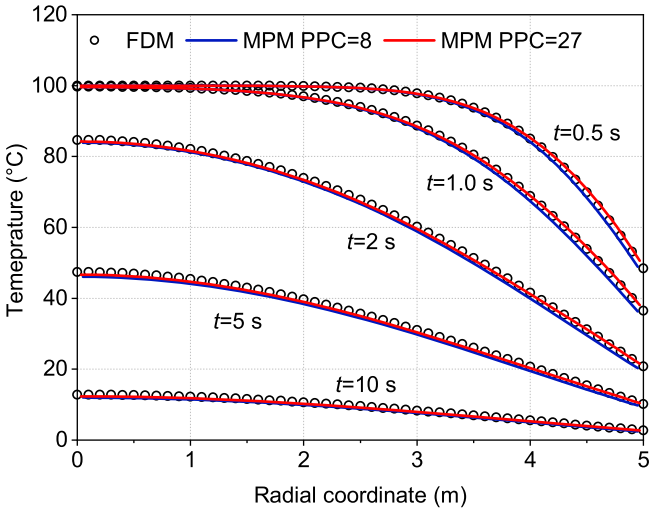

FIGURE 17 | Cooling of a sphere: comparison of temperature along the radial direction solved by MPM and FDM at $t = 0.5$, 1.0, 2.0, 5.0, and 10.0 s.

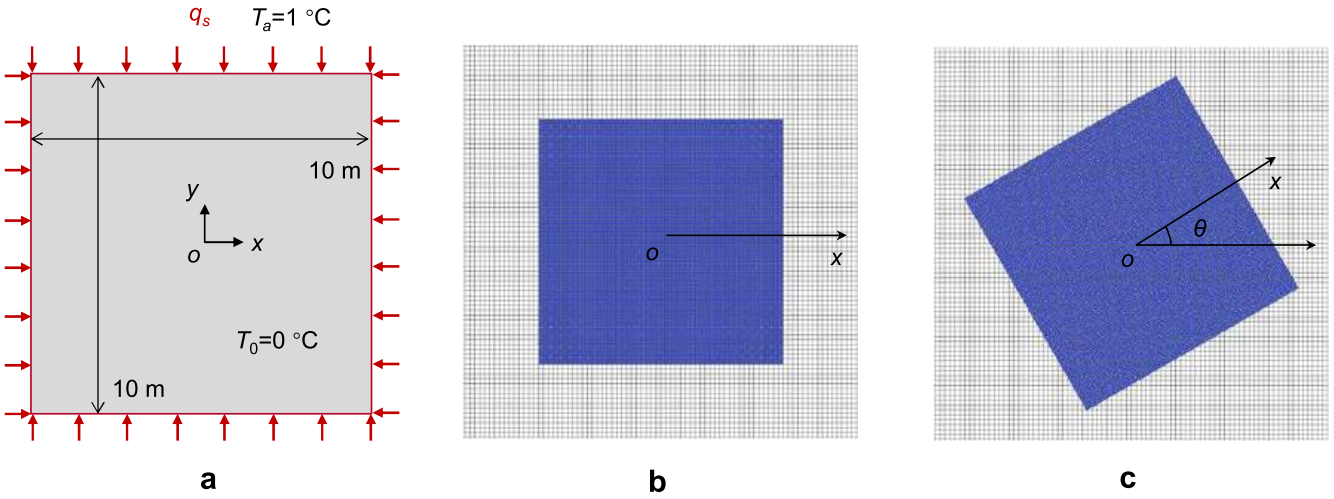

FIGURE 18 | Heating of a rotating square block: (a) geometry, initial and boundary conditions, (b) conforming boundary condition, and (c) nonconforming boundary condition.

Figure 19a–d present the simulation results for cases with different rotation angles θ. For each case, we first show the temperature contour plot computed using the MPM at $t = 5$ s. Superimposed on these contours are the temperature iso-lines (0.3, 0.5, 0.7, and 0.9°C) calculated by both MPM and the FDM for direct comparison. Additionally, the temporal evolution of the temperature profiles along the horizontal central axis of the square, obtained from both the MPM and FDM at $t = 1$, 5, 10, and 50 s, is compared. Moreover, the relative error between the two methods, defined as $(T_{\text{MPM}} - T_{\text{FDM}})/T_{\text{FDM}}$, is analyzed. The overall accuracy is quantified by computing the L2 norm of the relative error across all material points

$$\|e\|_{L^2} = \sqrt{\frac{1}{N_p}\sum_{p=1}^{N_p}(T_{\text{MPM}} - T_{\text{FDM}})_p^2}, \tag{45}$$

where N_p denotes the total number of material points.

The results, as shown in Figure 19a, demonstrate excellent agreement between the MPM and the FDM for the case of $\theta = 0°$ (i.e., conforming boundary configuration), with a very small error norm $\|e\|_{L^2}$. As the rotation angle increases, the MPM and FDM results remain in good overall agreement. However, a slight but consistent increase in $\|e\|_{L^2}$ is observed with larger θ. Notably, for $\theta = 45°$, the temperature iso-lines exhibit some spatial oscillations, and the spatial distribution of the relative error exhibits a distinct checkerboard pattern. This pattern is attributed to the suboptimal distribution

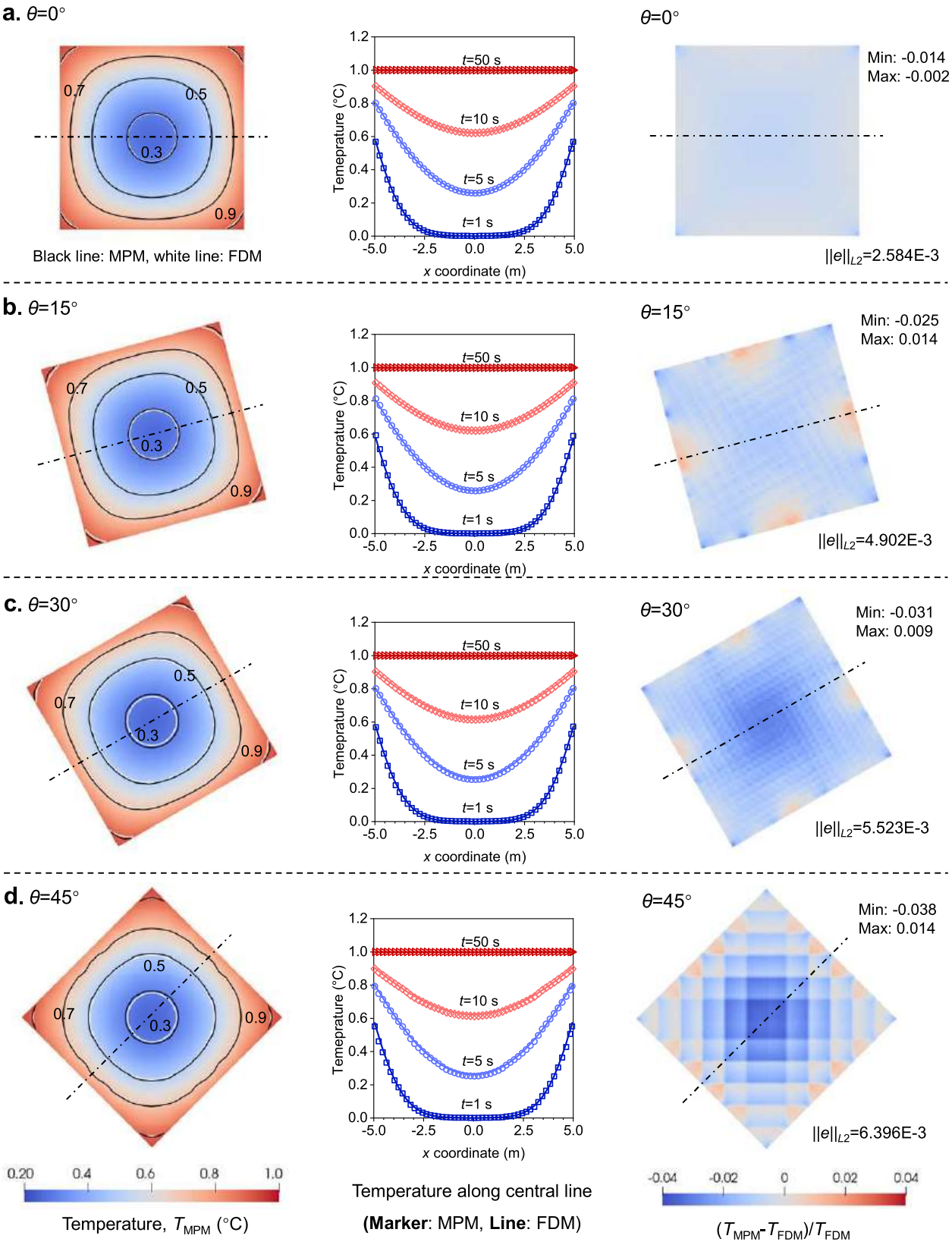

FIGURE 19 | Heating of a rotating square block: simulation results for different rotation angles: (a) $\theta = 0°$, (b) $\theta = 15°$, (c) $\theta = 30°$, and (d) $\theta = 45°$. The first column shows the temperature contours simulated by MPM with VHFM at $t = 5$ s, where the black and white isothermal lines represent MPM and FDM results, respectively. The second column compares the temperature distribution along the central line simulated by MPM and FDM at $t = 1, 5, 10$, and 50 s. The third column presents the relative error of the MPM results compared to the FDM results at $t = 5$ s.

of material points relative to the background grid after a 45° rotation. As illustrated in Figure 20a, the rotated material points are distributed irregularly with respect to the computational grid. Most of these points are displaced from optimized integration points, the Gaussian points. It is also clear that some of the entire rows or columns of material points coincide with grid lines—positions where the integration accuracy is minimal. This suboptimal discretization is the primary cause of the checkerboard pattern observed in the error contour plot of Figure 19d.

Therefore, the increased error for larger rotation angles likely stems predominantly from the material points deviating from optimal integration points, rather than from inaccuracies inherent to the boundary condition imposition by the VHFM. To verify this, we simulated the $\theta = 45°$ case using a different, optimized material point configuration (referred to as MP Configuration B), shown in Figure 20b. This configuration was generated by first creating a regular distribution of material points (PPC = 4) across the entire background mesh and then removing points located in the region defined by $|x| + |y| > 5\sqrt{2}$. Thus, MP Configuration B models the same physical domain as Configuration A (Figure 20a) but with a more favorable material point distribution. The simulation results using Configuration B, presented in Figure 21, show an error distribution and magnitude similar to those of the conforming case ($\theta = 0°$) in Figure 19a. This confirms that with an optimized internal discretization, nonconforming boundaries can yield accuracy comparable to conforming ones. It is important to note that even the original MP Configuration A maintains an error of the same order of magnitude as the conforming boundary case.

The above analysis pertains to Scenario A, which involves fixed, nonconforming boundaries. We now present results for Scenario B, where heat transfer occurs concurrently with the rigid-body rotation of the square. Figure 22 compares the temperature contours and relative error distributions (at $t = 5$ s) for four different rotational velocities. The results show that the errors remain very small in all cases, with $\|e\|_{L^2}$ norms on par with those of the static conforming boundary case.

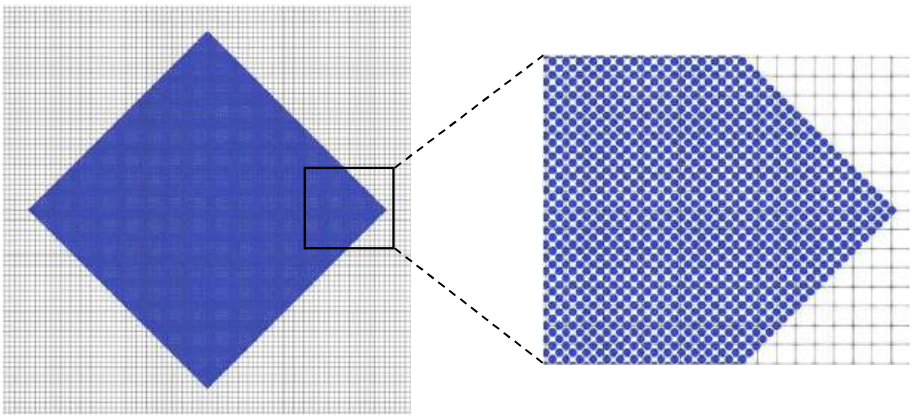

a. MP configuration A

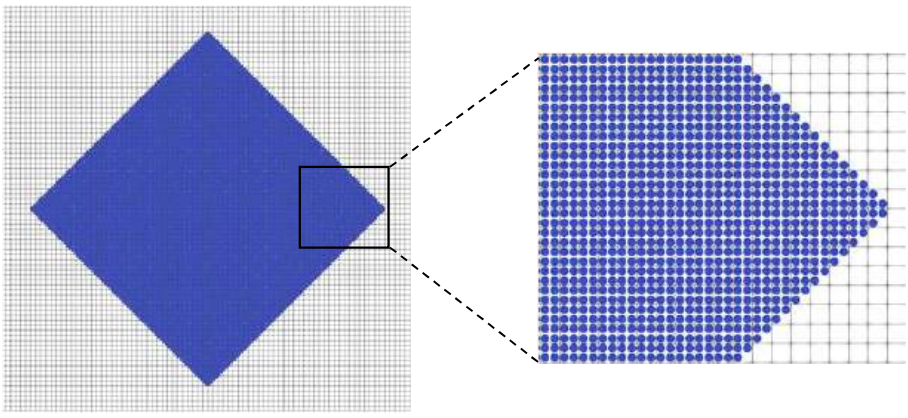

b. MP configuration B

FIGURE 20 | Heating of a rotating square block: (a) MP Configuration A—suboptimal MP distribution; (b) MP Configuration B – optimal MP distribution.

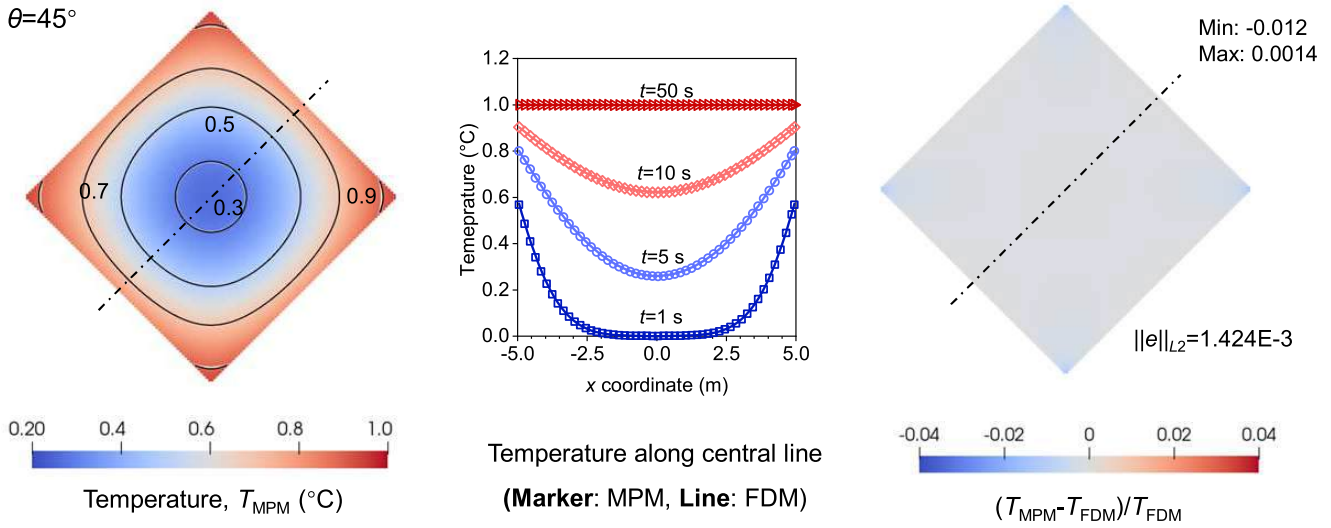

FIGURE 21 | Heating of a rotating square block: simulation results for $\theta = 45°$ using MP Configuration B.

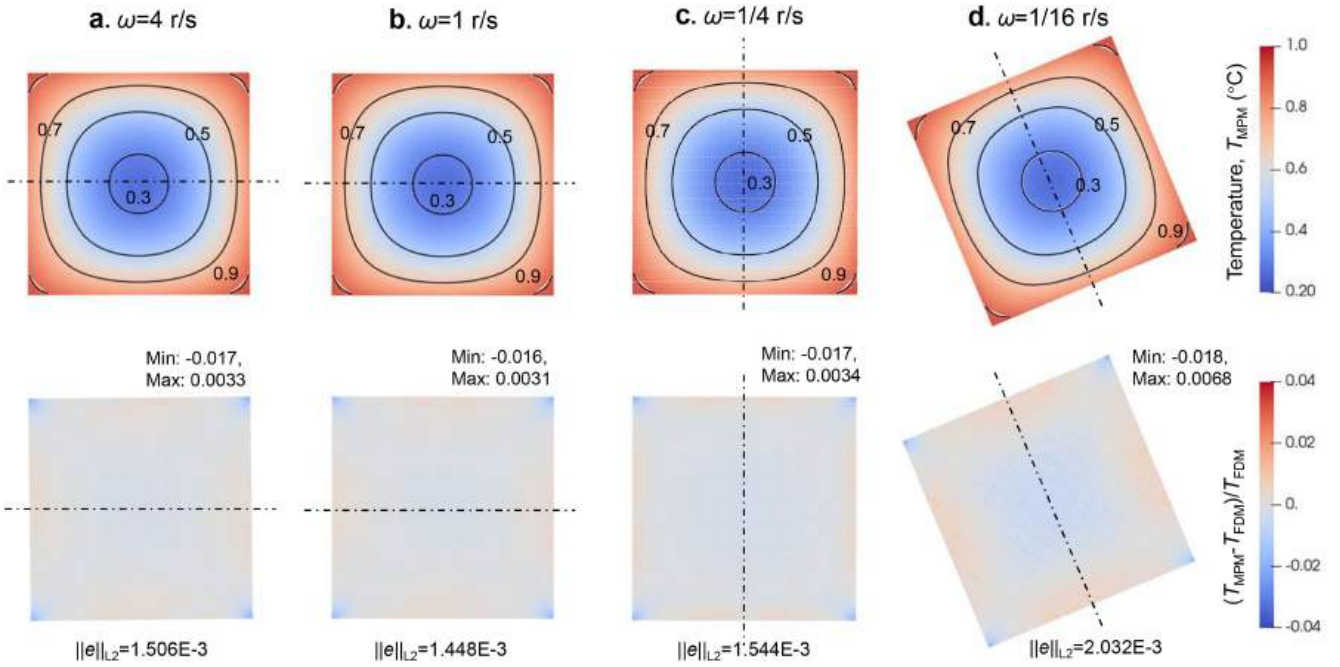

FIGURE 22 | Heating of a rotating square block: temperature and relative error contours with different resolution rate: (a) $\omega = 4$ r/s, (b) $\omega = 1$ r/s, (c) $\omega = 1/4$ r/s, and (d) $\omega = 1/16$ r/s.

This demonstrates that the proposed method remains highly accurate for simulating convective heat transfer even under dynamically evolving boundary conditions.

4.5 | Moving Boundary Example: Cooling a Rotating Fan

In the final example, we simulate a cooling problem of a rotating fan. The geometry of the fan is shown in Figure 23a, and its topological relationship with the background grid is illustrated in Figure 23b. The initial temperature of the fan is set to $T_0 = 100°C$, while the ambient temperature is $T_a = 0°C$. The convective heat transfer coefficient is prescribed as $\gamma = 1\ \mathrm{W/(m^2 \cdot °C)}$. The fan rotates about its center with a constant angular velocity of $\omega = 1$ r/s. The material point coordinates are generated directly from the absolute pixel coordinates of the input image. A background grid with a cell size of $h_e = 0.1$ m is first employed, with PPC = 4. The time step is chosen as $\Delta t = 5 \times 10^{-3}$ s.

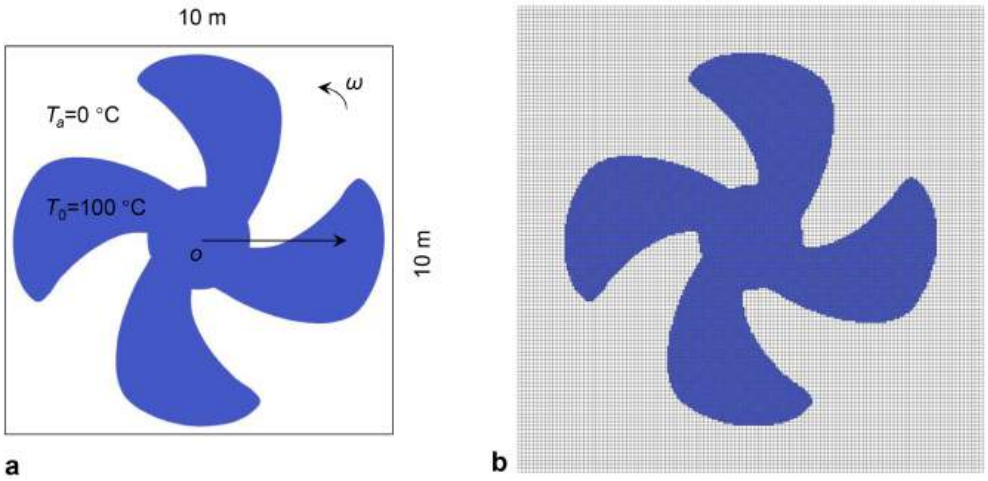

FIGURE 23 | Cooling of a rotating fan: (a) geometry of the fan and (b) material discretizations.

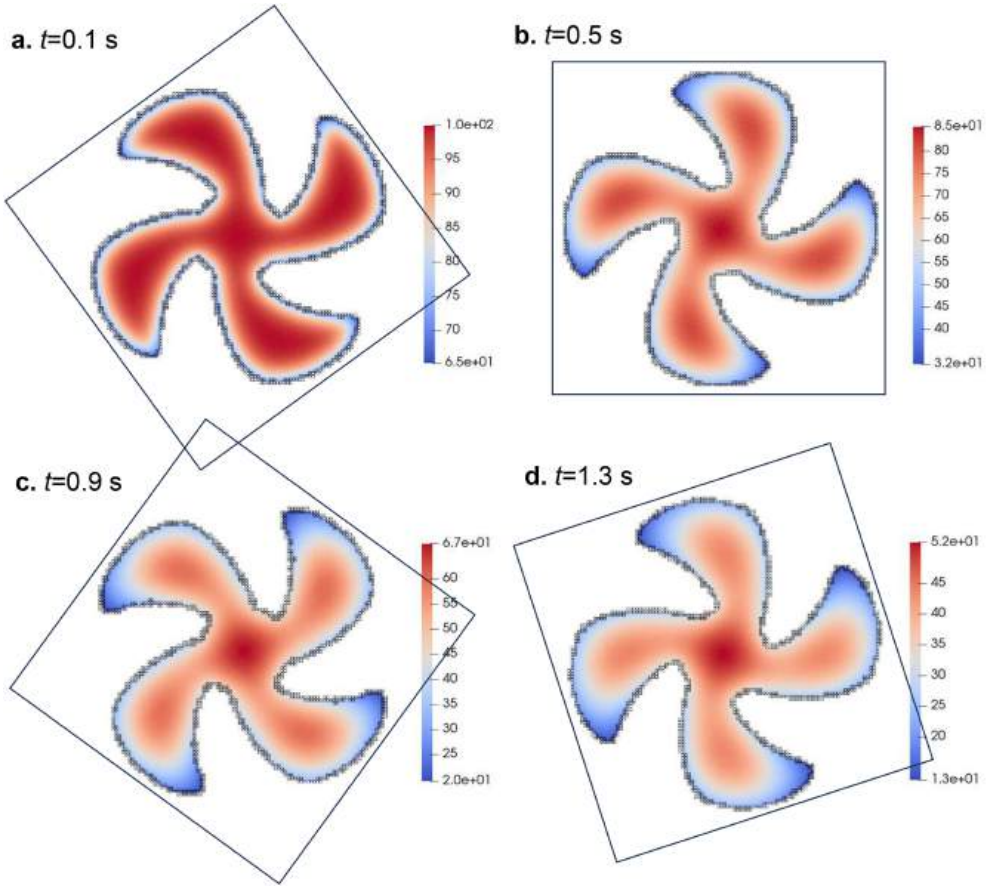

FIGURE 24 | Cooling of a rotating fan: Simulation results at different time instances.

Figure 24 presents the temperature contours at different time instants together with the detected surface nodes. The results exhibit a smooth temperature distribution, and the surface node detection remains reasonable and stable throughout the rotational process. Since no analytical solution is available for validation, additional simulations are conducted using a coarser grid ($h_e = 0.2$ m) and a finer grid ($h_e = 0.05$ m) to examine solution consistency and convergence. The corresponding time steps are set to $\Delta t = 2 \times 10^{-2}$ s and $\Delta t = 1.25 \times 10^{-3}$ s, respectively. Figure 25a–c compare the temperature distributions at $t = 0.5$ s for the three mesh resolutions. Good agreement is observed in both the overall temperature patterns and magnitudes. In addition, the temperature evolution at the center of the fan is examined, as shown in Figure 25d.

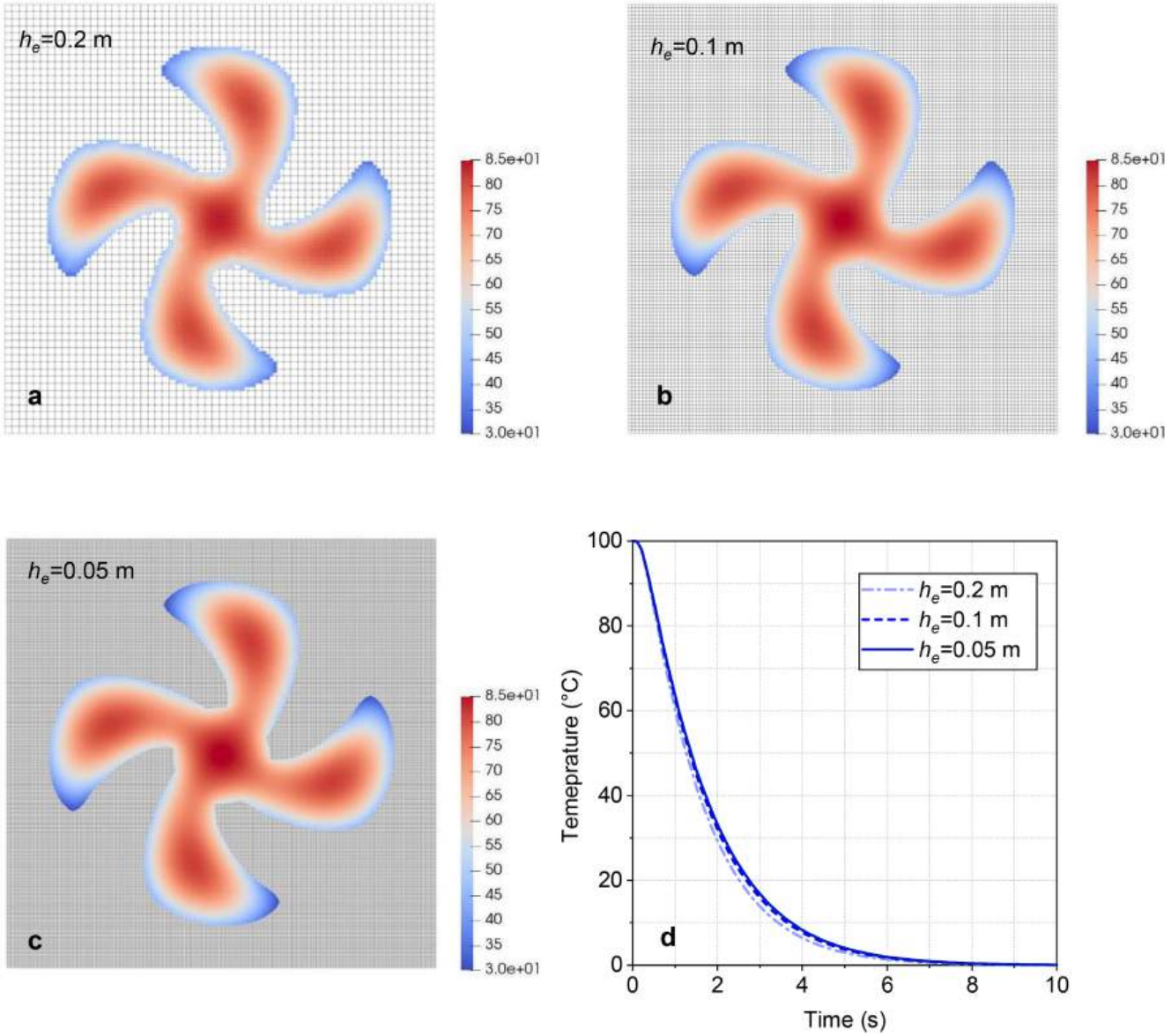

FIGURE 25 | Cooling of a rotating fan: Mesh sensitivity analysis. (a–c) Temperature distribution at $t = 0.5$ s for mesh sizes $h_e = 0.1$ m, $h_e = 0.05$ m, and $h_e = 0.025$ m, respectively; (d) Temperature evolution at the center of the fan for different mesh sizes.

The temperature decreases from 100°C to 0°C, and as the mesh is refined, the temperature histories converge to nearly a single curve.

This example demonstrates that the proposed VHFM is capable of accurately and robustly handling complex geometries and evolving boundary configurations.

4.6 | Large Deformation Example: Heating of a Collapsing Soil Column

Finally, we present a soil column collapse example to demonstrate the applicability of the proposed method to large deformation scenarios. A soil column of dimensions 2 m × 2 m is considered, as illustrated in Figure 26. For the mechanical part, we employ the standard MPM with linear shape functions. The particle velocity is updated using the FLIP scheme with a PIC damping ratio of 0.05, while the stress update follows the MUSL scheme. The constitutive model is elastic-perfectly plastic with the Mohr–Coulomb yield criterion. For illustrative purposes, the following virtual material parameters are adopted: elastic modulus $E = 1 \times 10^7$ Pa, Poisson's ratio $\nu = 0$, soil cohesion $c = 10$ Pa, friction angle

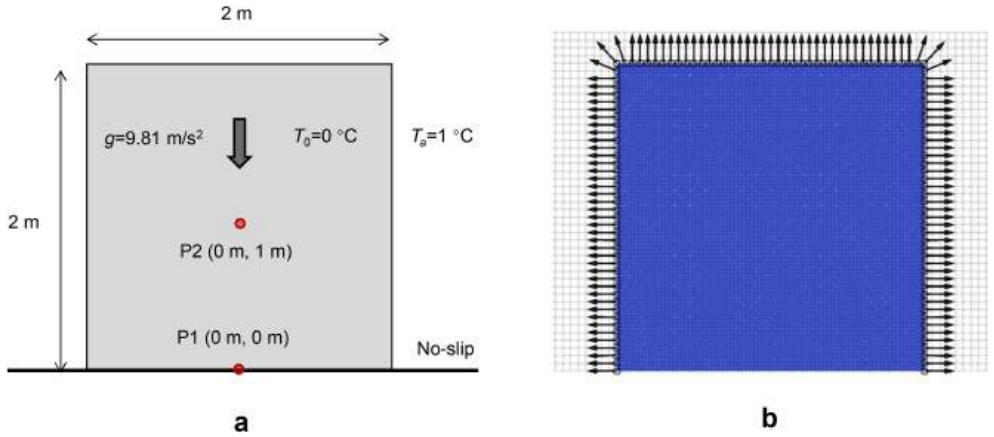

FIGURE 26 | Heating of a collapsed soil column: (a) model setup and (b) model discretizations, detected surface node and surface normal at the initial configuration.

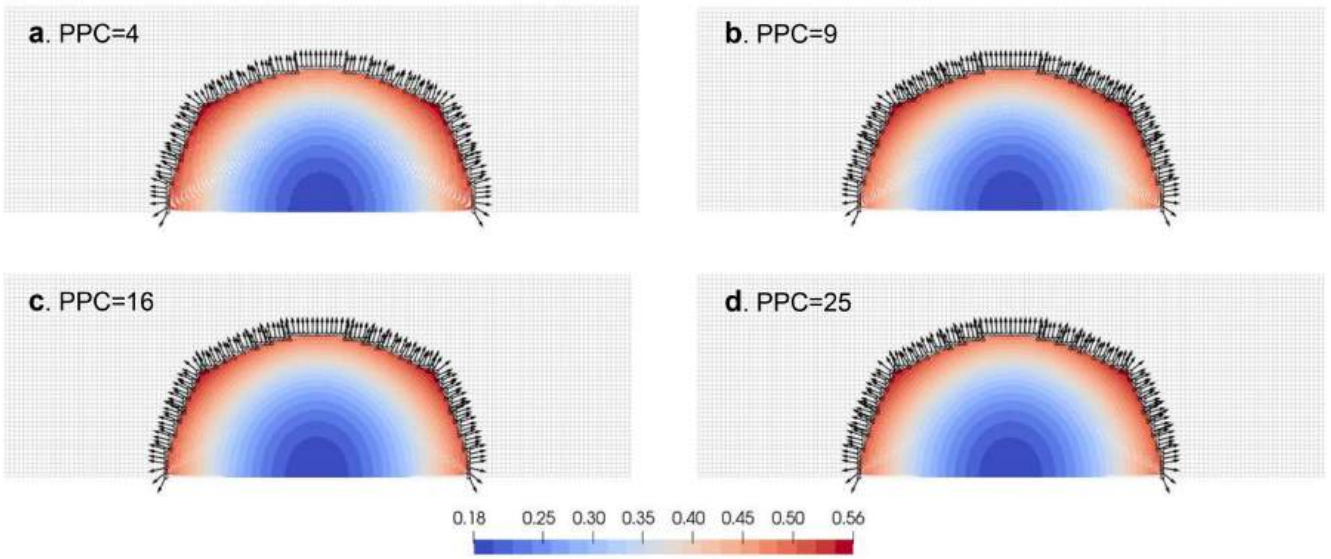

FIGURE 27 | Heating of a collapsed soil column: comparison of simulated temperature ans surface normal at $t = 0.5$ s for different cases with (a) PPC = 4, (b) PPC = 9, PPC = 16, and PPC = 25.

$\varphi = 30°$, and density $\rho = 2000$ kg/m^3. The thermal properties are set as follows: heat capacity $\rho c = 1$ J/(m^3·°C) and thermal conductivity $\kappa = 1$ W/(m·°C). The initial temperature of the soil column is $T_0 = 0$°C, the ambient temperature is $T_a = 1$°C, and the convective heat transfer coefficient is set to 1 W/(m^2·°C). Other thermal effects, such as thermal expansion and thermal dissipation, are neglected. Gravity is set as 9.81 m/s^2, and a no-slip boundary condition is applied at the bottom.

Figure 26a shows the initial geometry, and Figure 26b presents the computed surface normal for a mesh size of 0.1 m. We test four cases with PPC values of 4, 9, 16, and 25. Figures 27 and 28 compare the temperature distributions and computed surface normals at $t = 0.5$ and $t = 2.0$ s, respectively. At $t = 0.5$ s, where deformation is relatively small, all PPC values yield accurate surface normals and nearly identical temperature fields. However, at $t = 2.0$ s, when deformation is severe, the surface particles become very sparse in the PPC = 4 and 9 cases, with some cells even becoming empty. This leads to inaccuracies in the identification of surface nodes and the computation of surface normals, consequently causing abnormal temperature field solutions. Employing larger PPC values (e.g., 16 and 25) effectively mitigates this issue. As shown in Figure 28c,d, both the temperature field and the surface normal results for PPC = 16 and 25 are regular and in good agreement.

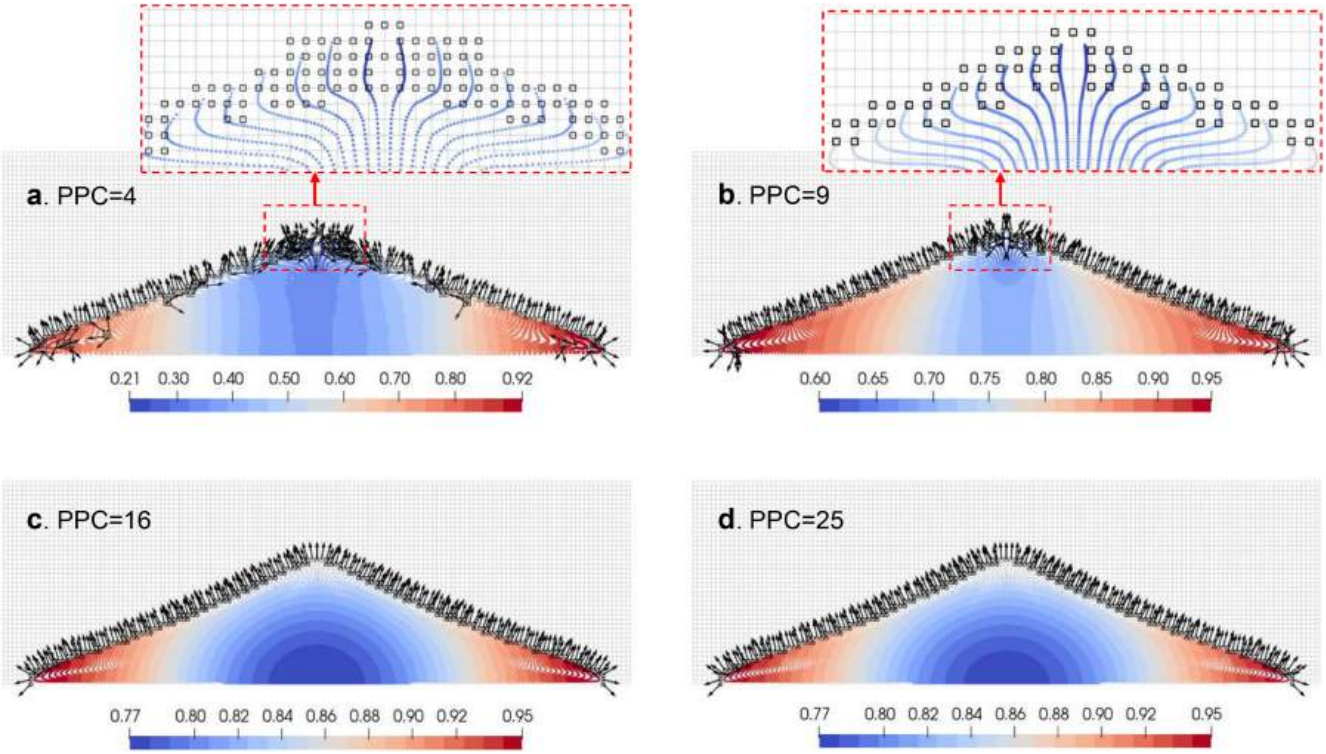

FIGURE 28 | Heating of a collapsed soil column: comparison of simulated temperature and surface normal at $t = 2$ s for different cases with (a) PPC = 4, (b) PPC = 9, PPC = 16, and PPC = 25.

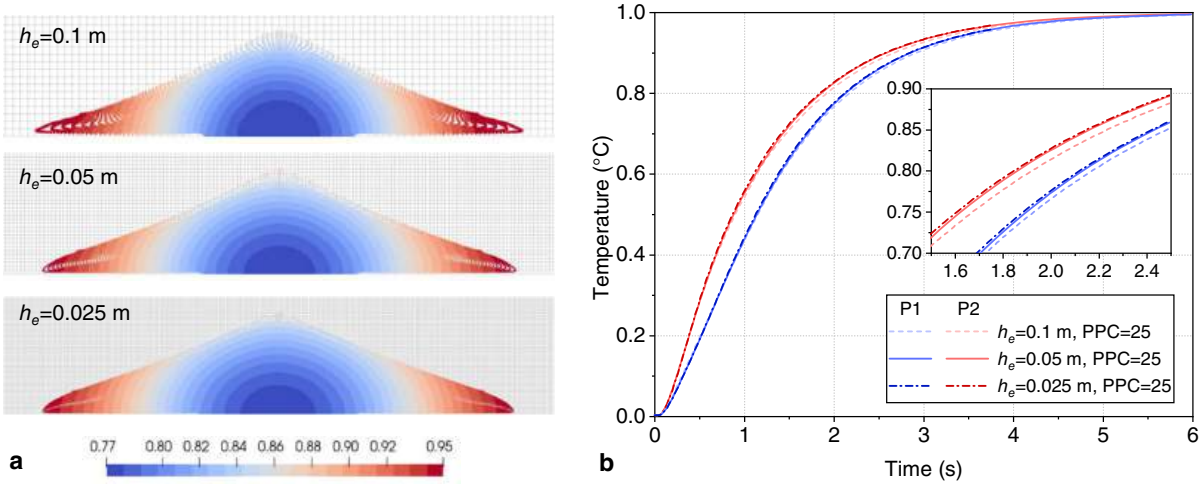

FIGURE 29 | Heating of a collapsed soil column: (a) comparison of temperature contours for different mesh sizes at $t = 2$ s and (b) comparison of temperature evolution at P1 and P2.

Furthermore, we conduct a mesh convergence study, testing three mesh sizes of 0.1, 0.05, and 0.025 m, all with PPC = 25. Figure 29a compares the temperature fields at $t = 2.0$ s for the three meshes, showing consistent results. Figure 29b provides a quantitative comparison of the temperature evolution at two monitoring points, P1 and P2 (as indicated in Figure 26a). The results for the three meshes are again consistent and exhibit clear convergence.

This example demonstrates that when large deformation leads to sparse surface particles, the method of constructing the surface normal based on volume fraction or mass gradient may produce significant distortion. Increasing the particle distribution density (i.e., using a larger PPC) can effectively resolve this issue. Nevertheless, it is important to note that when particles become sparse, not only the construction of surface normals but also the evaluation of temperature gradients deteriorates, resulting in a distorted temperature field. Therefore, a sufficiently high particle distribution density

is necessary for such large deformation problems. Future work should further improve the accuracy of temperature field solutions under sparse particle conditions, for instance, by adopting more robust surface normal construction techniques or higher-order shape functions.

5 | Conclusions

This study has presented a virtual heat flux Method (VHFM) for the simple and accurate imposition of Neumann-type thermal boundary conditions within the MPM framework. The method fundamentally addresses the challenge of non-conforming boundaries by recasting the boundary flux integral into a volumetric term via a conceptually simple virtual flux field.

The proposed VHFM offers several key advantages. (1) It removes the necessity for explicit boundary tracking, surface reconstruction, or the use of specialized boundary particles, preserving the inherent efficiency of the standard MPM algorithm. (2) It achieves accuracy on par with direct nodal imposition in conforming cases and delivers superior, consistent results for nonconforming, curved, and moving boundaries where the conventional boundary-particle method fails. (3) The formulation provides a unified framework extensible to other Neumann conditions (e.g., traction, fluid flux) through the appropriate construction of the virtual field. (4) Our numerical experiments, spanning 1D to 3D, from simple geometries to a complex rotating fan, and a large-deformation column collapse example, demonstrate the method's efficacy under various nonconforming and evolving boundary conditions.

Despite its satisfactory performance in the tested scenarios, the current formulation of the VHFM has certain limitations that warrant further investigation. First, it adopts the gradient of mass to evaluate the surface normal, which may not work when the particle distribution becomes sparse under large deformations. It can be addressed by increasing the particle distribution density, but this inevitably increases the computational cost. Second, the current framework assumes boundary evolution that is continuous in topology. Its efficacy for problems involving rapid topological changes, such as fracture, fragmentation, or the merging of material bodies, has not been established. The construction of a stable virtual domain surrounding dynamically changing topological features presents an open challenge. Third, while the extension to coupled problems is conceptually clear, its implementation in fully implicit, strongly coupled multiphysics systems (e.g., thermo-hydro-mechanical, where the boundary flux depends on the evolving pressure or deformation field) needs to be rigorously tested. The interaction between the virtual flux and the nonlinear solution process in such coupled regimes requires additional analysis to ensure stability and consistency. Therefore, in future work, more advanced surface detection and surface normal construction approaches should be explored, and the extension of the VHFM to fully coupled THM problems should be carefully validated.

Nomenclature

CFL	Courant-Friedrichs-Lewy condition
FDM	Finite Difference Method
FLIP	Fluid-Implicit Particle
MPM	Material Point Method
MUSL	Modified Update Stress Last method
NB	Node Boundary (boundary condition imposition method)
PB	Particle Boundary (boundary condition imposition method)
PIC	Particle-In-Cell
PPC	Particles per cell
RMSE	Root Mean Square Error
THM	Thermo-Hydro-Mechanical
VHFM	Virtual Heat Flux Method

Greek Symbols

α	Thermal diffusivity, $\alpha = \kappa/(\rho c)$ (m^2/s)
γ	Convective heat transfer coefficient ($W/(m^2 \cdot °C)$)
δT, δT_I, δT_p	Admissible virtual temperature field, virtual temperature at node I and particle p (°C)
ε_{err}	Root mean square error (RMSE)
η	Volume fraction threshold for surface detection
θ_{err}	Angular error of surface normal (°)
κ, $\boldsymbol{\kappa}$	Scalar and tensor thermal conductivity ($W/(m \cdot °C)$)
$\overline{\mu}$	Indicator function for virtual domain
ρ	Material density (kg/m^3)
ϕ	Unified scalar field for normal estimation
Ω, $\overline{\Omega}$	Physical material domain, virtual domain
$\partial\Omega$, $\partial\Omega_q$, $\partial\Omega_T$	Boundary of physical domain, heat flux boundary, temperature boundary
ω	Angular velocity (r/s or rad/s)

Roman Symbols

A_p	Effective surface area associated with a boundary particle (m^2)
c, ρc	Specific heat capacity ($J/(kg \cdot °C)$), volumetric heat capacity ($J/(°C \cdot m^3)$)
C_I, C_{IJ}	Lumped nodal heat capacity, consistent nodal heat capacity matrix (J/°C)
$\mathcal{E}_I^{\text{int}}$, $\mathcal{E}_I^{\text{ext}}$	Internal and external heat contribution at node I (W)
$\widetilde{\mathcal{E}}_I^{\text{int}}$, $\widetilde{\mathcal{E}}_I^{\text{ext}}$	Modified internal/external heat contribution under VHFM (W)
h_e	Element/mesh size (m)
$h_{\min}$	Minimum mesh size (m)
h_p, h_I	Boundary characteristic thickness at particle p and node I (m)
m, m_I, m_p	Mass, nodal mass, particle mass (kg)
$\boldsymbol{n}$, $\boldsymbol{n}_p$	Outward unit normal vector
$\mathcal{N}_1$	Surface node set
$\mathcal{P}_1$, $\mathcal{P}_2$	Surface particle set, non-surface particle set
Q	Volumetric heat source (W/m^3)
$\boldsymbol{q}$, $\overline{\boldsymbol{q}}$	Heat flux vector, virtual heat flux vector (W/m^2)
$\hat{q}$	Prescribed inward heat flux (W/m^2)
S_{Ip}	MPM shape function at node I associated with particle p
T	Temperature (°C)
$\overline{T}$	Auxiliary temperature field in virtual domain (°C)
T_a	Ambient temperature (°C)
$\hat{T}$	Prescribed temperature on Dirichlet boundary (°C)

$\mathcal{T}$	Time interval $[0, t]$ (s)
Δt	Time step size (s)
Δt_{cr}	Critical time step (s)
V, V_p, V_c	Volume, particle volume, cell volume (m^3)
$V_{p \in c}$	Total particle volume in a cell (m^3)

Subscripts and superscripts

$\square_p$	Quantity associated with material point/particle p
$\square_I$	Quantity associated with grid node I
$\square^k$	Quantity at time step k

Author Contributions

Jidu Yu: conceptualization; methodology; software; data curation; investigation; validation; formal analysis; visualization; writing – original draft.

Acknowledgments

This work was financially supported by the National Natural Science Foundation of China (# 52439001), the Research Grants Council of Hong Kong (GRF 16208224, 16217225, CRF C7085-24G, RIF R6008-24, TRS T22-607/24N, and T22-606/23-R), and the State Key Laboratory of Climate Resilience for Coastal Cities (SKLCRCC) (via Project ITC-SKLCRCC26EG01). Jidu Yu is grateful to Prof. Kenichi Soga, Dr. Bodhinanda Chandra, and Dr. Joel Given of the University of California, Berkeley, for their invaluable discussions and suggestions on this work.

Funding

This work was supported by the National Natural Science Foundation of China (Grant No. 52439001), the Research Grants Council of Hong Kong (Grant Nos. 16208224, 16217225, C7085-24G, R6008-24, T22-607/24N, T22-606/23-R), and the State Key Laboratory of Climate Resilience for Coastal Cities (Grant No. ITC-SKLCRCC26EG01).

Conflicts of Interest

The authors declare no conflicts of interest.

Data Availability Statement

The data that support the findings of this study are available from the corresponding author upon reasonable request.

References

1. S. G. Bardenhagen and E. M. Kober, "The Generalized Interpolation Material Point Method," *Computer Modeling in Engineering and Sciences* 5, no. 6 (2004): 477–496.

2. D. Sulsky, Z. Chen, and H. L. Schreyer, "A Particle Method for History-Dependent Materials," *Computer Methods in Applied Mechanics and Engineering* 118, no. 1 (1994): 179–196, https://doi.org/10.1016/0045-7825(94)90112-0.

3. D. Sulsky, S.-J. Zhou, and H. L. Schreyer, "Application of a Particle-In-Cell Method to Solid Mechanics," *Computer Physics Communications* 87, no. 1 (1995): 236–252, https://doi.org/10.1016/0010-4655(94)00170-7.

4. A. Sadeghirad, R. M. Brannon, and J. Burghardt, "A Convected Particle Domain Interpolation Technique to Extend Applicability of the Material Point Method for Problems Involving Massive Deformations," *International Journal for Numerical Methods in Engineering* 86, no. 12 (2011): 1435–1456.

5. K. Soga, E. Alonso, A. Yerro, K. Kumar, and S. Bandara, "Trends in Large-Deformation Analysis of Landslide Mass Movements With Particular Emphasis on the Material Point Method," *Géotechnique* 66, no. 3 (2016): 248–273, https://doi.org/10.1680/jgeot.15.LM.005.

6. J. Tao, H. Zhang, Y. Zheng, and Z. Chen, "Development of Generalized Interpolation Material Point Method for Simulating Fully Coupled Thermomechanical Failure Evolution," *Computer Methods in Applied Mechanics and Engineering* 332 (2018): 325–342, https://doi.org/10.1016/j.cma.2017.12.014.

7. S. Zhao, H. Chen, and J. Zhao, "Multiscale Modeling of Freeze-Thaw Behavior in Granular Media," *Acta Mechanica Sinica* 39, no. 1 (2022): 722195, https://doi.org/10.1007/s10409-022-22195-x.

8. X. Lei, S. He, A. Abed, X. Chen, Z. Yang, and Y. Wu, "A Generalized Interpolation Material Point Method for Modelling Coupled Thermo-Hydro-Mechanical Problems," *Computer Methods in Applied Mechanics and Engineering* 386 (2021): 114080, https://doi.org/10.1016/j.cma.2021.114080.

9. J. Yu, W. Liang, and J. Zhao, "Enhancing Dynamic Modeling of Porous Media With Compressible Fluid: A Thm Material Point Method With Improved Fractional Step Formulation," *Computer Methods in Applied Mechanics and Engineering* 444 (2025): 118100.

10. X. Lei, S. He, X. Chen, Z. Yang, Y. Dong, and L. Wang, "Mpm Simulation of Frictional Heating–Induced Hypermobility of Landslides," *Landslides* 21, no. 9 (2024): 2273–2287.

11. N. M. Pinyol, M. Alvarado, E. E. Alonso, and F. Zabala, "Thermal Effects in Landslide Mobility," *Géotechnique* 68, no. 6 (2018): 528–545, https://doi.org/10.1680/jgeot.17.P.054.

12. X. Lei, S. He, C. Qin, J. Zhao, G. G. Zhou, and L. Ming, "A Thm-Coupled Mpm Framework for Modelling Rock-Ice Avalanches," *Computers and Geotechnics* 188 (2025): 107603.

13. J. Yu, J. Zhao, W. Liang, and S. Zhao, "A Semi-Implicit Material Point Method for Coupled Thermo-Hydro-Mechanical Simulation of Saturated Porous Media in Large Deformation," *Computer Methods in Applied Mechanics and Engineering* 418 (2024): 116462, https://doi.org/10.1016/j.cma.2023.116462.

14. J. Yu, J. Zhao, K. Soga, S. Zhao, and W. Liang, "A Fully Coupled Thmc-Mpm Framework for Modeling Phase Transition and Large Deformation in Methane Hydrate-Bearing Sediment," *Journal of the Mechanics and Physics of Solids* 206 (2026): 106368.

15. F. Sun, G. Wang, L. Zhang, et al., "Multiphysics Coupling Material Point Method for Modelling Frost Heave of Rock Slope," *Computers and Geotechnics* 148 (2022): 104793, https://doi.org/10.1016/j.compgeo.2022.104793.

16. J. Yu, J. Zhao, W. Liang, and S. Zhao, "Multiscale Modeling of Coupled Thermo-Hydro-Mechanical Behavior in Ice-Bonded Granular Media Subject to Freeze-Thaw Cycles," *Computers and Geotechnics* 171 (2024): 106349, https://doi.org/10.1016/j.compgeo.2024.106349.

17. J. Yu, J. Zhao, S. Zhao, and W. Liang, "Thermo-Hydro-Mechanical Coupled Material Point Method for Modeling Freezing and Thawing of Porous Media," *International Journal for Numerical and Analytical Methods in Geomechanics* 48, no. 13 (2024): 3308–3349, https://doi.org/10.1002/nag.3794.

18. S. Kularathna, W. Liang, T. Zhao, B. Chandra, J. Zhao, and K. Soga, "A Semi-Implicit Material Point Method Based on Fractional-Step Method for Saturated Soil," *International Journal for Numerical and Analytical Methods in Geomechanics* 45, no. 10 (2021): 1405–1436, https://doi.org/10.1002/nag.3207.

19. X. Zheng, F. Pisanò, P. J. Vardon, and M. A. Hicks, "Fully Implicit, Stabilised MPM Simulation of Large-Deformation Problems in Two-Phase Elastoplastic Geomaterials," *Computers and Geotechnics* 147 (2022): 104771, https://doi.org/10.1016/j.compgeo.2022.104771.

20. Y. Yamaguchi, S. Moriguchi, and K. Terada, "Extended B-Spline-Based Implicit Material Point Method," *International Journal for Numerical Methods in Engineering* 122, no. 7 (2021): 1746–1769, https://doi.org/10.1002/nme.6598.

21. W. M. Coombs, "Ghost Stabilisation of the Material Point Method for Stable Quasi-Static and Dynamic Analysis of Large Deformation Problems," *International Journal for Numerical Methods in Engineering* 124, no. 21 (2023): 4841–4875, https://doi.org/10.1002/nme.7332.

22. P. Hernández-Becerro, D. Spescha, and K. Wegener, "Model Order Reduction of Thermo-Mechanical Models With Parametric Convective Boundary Conditions: Focus on Machine Tools," *Computational Mechanics* 67, no. 1 (2021): 167–184.

23. B. Roe, R. Jaiman, A. Haselbacher, and P. H. Geubelle, "Combined Interface Boundary Condition Method for Coupled Thermal Simulations," *International Journal for Numerical Methods in Fluids* 57, no. 3 (2008): 329–354.

24. S. Colston and I. N. Williams, "Convectively Induced Secondary Circulations and Wind-Driven Heat Fluxes in the Surface Energy Balance Over Land," *Geophysical Research Letters* 51, no. 20 (2024): e2024GL110565.

25. J. Hjort, D. Streletskiy, G. Doré, Q. Wu, K. Bjella, and M. Luoto, "Impacts of Permafrost Degradation on Infrastructure," *Nature Reviews Earth & Environment* 3, no. 1 (2022): 24–38, https://doi.org/10.1038/s43017-021-00247-8.

26. H. Tounsi, A. Rouabhi, M. Tijani, and F. Guérin, "Thermo-Hydro-Mechanical Modeling of Artificial Ground Freezing: Application in Mining Engineering," *Rock Mechanics and Rock Engineering* 52, no. 10 (2019): 3889–3907, https://doi.org/10.1007/s00603-019-01786-9.

27. Y. Liang, J. Given, and K. Soga, "The Imposition of Nonconforming Neumann Boundary Condition in the Material Point Method Without Boundary Representation," *Computer Methods in Applied Mechanics and Engineering* 404 (2023): 115785, https://doi.org/10.1016/j.cma.2022.115785.

28. B. Curless and M. Levoy, "A Volumetric Method for Building Complex Models From Range Images," in *Proceedings of the 23rd Annual Conference on Computer Graphics and Interactive Techniques* (Association for Computing Machinery, 1996), 303–312.

29. B. Chandra, V. Singer, T. Teschemacher, R. Wüchner, and A. Larese, "Nonconforming Dirichlet Boundary Conditions in Implicit Material Point Method by Means of Penalty Augmentation," *Acta Geotechnica* 16, no. 8 (2021): 2315–2335.

30. I. K. Al-Kafaji, *Formulation of a Dynamic Material Point Method (Mpm) for Geomechanical Problems*. Ph.D. thesis (Universitätsbibliothek der Universität Stuttgart, 2013).

31. W. Liang, H. Fang, Z.-Y. Yin, and J. Zhao, "A Mortar Segment-To-Segment Frictional Contact Approach in Material Point Method," *Computer Methods in Applied Mechanics and Engineering* 431 (2024): 117294.

32. L. Wang, W. M. Coombs, C. E. Augarde, et al., "Modelling Screwpile Installation Using the MPM," *Procedia Engineering* 175 (2017): 124–132.

33. J. Given, Y. Liang, Z. Zeng, X. Zhang, and K. Soga, "The Virtual Stress Boundary Method to Impose Nonconforming Neumann Boundary Conditions in the Material Point Method," *Computational Particle Mechanics* 12, no. 6 (2025): 4725–4749.

34. S. Zhao, J. Zhao, and Y. Lai, "Multiscale Modeling of Thermo-Mechanical Responses of Granular Materials: A Hierarchical Continuum–Discrete Coupling Approach," *Computer Methods in Applied Mechanics and Engineering* 367 (2020): 113100, https://doi.org/10.1016/j.cma.2020.113100.

35. S. Bardenhagen, J. Brackbill, and D. Sulsky, "The Material-Point Method for Granular Materials," *Computer Methods in Applied Mechanics and Engineering* 187, no. 3–4 (2000): 529–541.

36. J. Li, R. Ni, Z. Zeng, and X. Zhang, "An Efficient Solid Shell Material Point Method for Large Deformation of Thin Structures," *International Journal for Numerical Methods in Engineering* 125, no. 1 (2024): e7359.

37. Y. Zhao, J. Choo, Y. Jiang, and L. Li, "Coupled Material Point and Level Set Methods for Simulating Soils Interacting With Rigid Objects With Complex Geometry," *Computers and Geotechnics* 163 (2023): 105708.

Appendix A

Analytical Solution for 1D Semi-Infinite Rod

The governing equation for 1D transient heat conduction is given by,

$$\frac{\partial T}{\partial t} = \alpha \frac{\partial^2 T}{\partial x^2}, \quad \text{for } x > 0,\ t > 0, \tag{A1}$$

where $\alpha = \kappa/(\rho c)$ is the thermal diffusivity. The initial condition is,

$$T(x, 0) = T_0, \quad \text{for } x \geq 0. \tag{A2}$$

Constant Heat Flux Boundary

The boundary condition at $x = 0$ is,

$$-\kappa \frac{\partial T}{\partial x}\Big|_{x=0} = q_s, \quad \text{for } t > 0. \tag{A3}$$

This problem can be solved using the Laplace transform method. Defining the transformed temperature as $\Theta(x, s) = \mathcal{L}\{T(x, t) - T_0\}$, the governing equation becomes,

$$\frac{d^2\Theta}{dx^2} - \frac{s}{\alpha}\Theta = 0. \tag{A4}$$

The solution satisfying the semi-infinite condition ($\Theta \to 0$ as $x \to \infty$) is,

$$\Theta(x, s) = A(s) \exp\left(-x\sqrt{\frac{s}{\alpha}}\right). \tag{A5}$$

Applying the transformed boundary condition from Equation (A3), $-\kappa \frac{d\Theta}{dx}\Big|_{x=0} = \frac{q_s}{s}$, yields,

$$A(s) = \frac{q_s}{\kappa s^{3/2}\sqrt{\alpha}}. \tag{A6}$$

Thus,

$$\Theta(x, s) = \frac{q_s}{\kappa\sqrt{\alpha}} \cdot \frac{\exp(-x\sqrt{s/\alpha})}{s^{3/2}}. \tag{A7}$$

The inverse Laplace transform of this expression leads to the solution,

$$T(x, t) = T_0 + \frac{2q_s}{\kappa}\sqrt{\frac{\alpha t}{\pi}} \exp\left(-\frac{x^2}{4\alpha t}\right) - \frac{q_s x}{\kappa} \operatorname{erfc}\left(\frac{x}{2\sqrt{\alpha t}}\right). \tag{A8}$$

Convective Heat Flux Boundary

The boundary condition at $x = 0$ is,

$$-\kappa \frac{\partial T}{\partial x}\Big|_{x=0} = \gamma(T_a - T(0,t)), \quad \text{for } t > 0. \tag{A9}$$

Again, using the Laplace transform with $\Theta(x,s) = \mathcal{L}\{T(x,t) - T_0\}$, the solution in the transformed domain is,

$$\Theta(x,s) = A(s)\exp\left(-x\sqrt{\frac{s}{\alpha}}\right). \tag{A10}$$

Applying the transformed boundary condition from Equation (A9), $-\kappa \frac{d\Theta}{dx}\Big|_{x=0} = \gamma\left(\frac{T_a - T_0}{s} - \Theta(0,s)\right)$, and solving for $A(s)$ gives,

$$A(s) = \frac{\gamma(T_a - T_0)/s}{\kappa\sqrt{s/\alpha} + \gamma}. \tag{A11}$$

Thus, the solution in the Laplace domain is,

$$\Theta(x,s) = \frac{\gamma(T_a - T_0)}{\kappa\sqrt{\alpha}} \cdot \frac{\exp(-x\sqrt{s/\alpha})}{\sqrt{s}(\sqrt{s} + \gamma/(\kappa\sqrt{\alpha}))}. \tag{A12}$$

Finding the inverse Laplace transform of this expression, typically by employing a table of Laplace transforms or the convolution theorem, yields the solution,

$$T(x,t) = T_0 + (T_a - T_0)\left[\operatorname{erfc}\left(\frac{x}{2\sqrt{\alpha t}}\right) - \exp\left(\frac{\gamma x}{\kappa} + \frac{\gamma^2 \alpha t}{\kappa^2}\right)\operatorname{erfc}\left(\frac{x}{2\sqrt{\alpha t}} + \frac{\gamma\sqrt{\alpha t}}{\kappa}\right)\right]. \tag{A13}$$

Appendix B

FDM Algorithm for 2D Circular Ring

For a 2D disk with a radius of R, the heat equation is expressed in polar coordinates (r, θ), where r is the radial distance and θ is the angular coordinate. Assuming symmetry in the angular direction (so T depends only on r and t), the heat equation simplifies to,

$$\frac{\partial T}{\partial t} = \alpha\left(\frac{\partial^2 T}{\partial r^2} + \frac{1}{r}\frac{\partial T}{\partial r}\right), \quad \text{for } R_1 \le r \le R_2\ ,\ t > 0. \tag{B1}$$

The initial condition is,

$$T(r,0) = T_0, \quad \text{for } R_1 \le r \le R_2. \tag{B2}$$

The convective heat flux boundary conditions at the inner ($r = R_1$) and outer boundary ($r = R_2$) are,

$$-\kappa \frac{\partial T}{\partial r}\Big|_{r=R_1} = \gamma\left[T(R_1,t) - T_a\right], \tag{B3}$$

$$-\kappa \frac{\partial T}{\partial r}\Big|_{r=R_2} = \gamma\left[T(R_2,t) - T_a\right]. \tag{B4}$$

The second-order central difference and forward Euler time integration scheme are used for spatial and temporal discretizations of the equation,

$$T_i^{k+1} = T_i^k + \alpha\Delta t\left(\frac{T_{i+1}^k - 2T_i^k + T_{i-1}^k}{\Delta r^2} + \frac{1}{r_i}\frac{T_{i+1}^k - T_{i-1}^k}{2\Delta r}\right), \tag{B5}$$

where T_i^k is the temperature at radial position r_i $(i = 0, 1, \ldots, N)$ and time step k, Δr is the radial step size, Δt is the time step size. The scheme is second-order in space and first-order in time.

At the inner and outer boundary, the second-order three-point one-Sided difference scheme is adopted,

$$\text{At } r = R_1 : \frac{3T_2^k - 4T_1^k + T_0^k}{2\Delta r} = \gamma(T_0^k - T_a) , \tag{B6}$$

$$\text{At } r = R_2 : \frac{3T_N^k - 4T_{N-1}^k + T_{N-2}^k}{2\Delta r} = \gamma(T_N^k - T_a) , \tag{B7}$$

From Equations (B6) and (B7), the prescribed boundary temperature T_0^k and T_N^k can be obtained.

For the constant heat flux boundary, it is only necessary to replace the boundary terms on the right-hand side of Equations (B6) and (B7) with the fixed value q_s.

Appendix C

FDM Algorithm for 3D Sphere

For a sphere of radius R with convective cooling, the 1D radial heat equation in spherical coordinates is,

$$\frac{\partial T}{\partial t} = \alpha\left(\frac{\partial^2 T}{\partial r^2} + \frac{2}{r}\frac{\partial T}{\partial r}\right), \quad 0 \le r < R, \ t > 0. \tag{C1}$$

The boundary conditions is

$$\left.\frac{\partial T}{\partial r}\right|_{r=0} = 0, \quad -\kappa \left.\frac{\partial T}{\partial r}\right|_{r=R} = \gamma\left[T(R,t) - T_a\right], \tag{C2}$$

and the initial condition is,

$$T(r,0) = T_0. \tag{C3}$$

Similarly, using the second-order central difference and forward Euler time integration scheme for spatial and temporal discretizations of the equation,

$$T_i^{k+1} = T_i^k + \alpha\Delta t\left[\frac{T_{i+1}^k - 2T_i^k + T_{i-1}^k}{\Delta r^2} + \frac{2}{r_i}\frac{T_{i+1}^k - T_{i-1}^k}{2\Delta r}\right]. \tag{C4}$$

At the inner boundary, using symmetry $T_0^k = T_2^k$,

$$T_1^{k+1} = T_1^k + 3\alpha\Delta t\frac{T_2^k - T_1^k}{\Delta r^2}. \tag{C5}$$

At the outer boundary, the second-order three-point one-Sided difference scheme is adopted,

$$-\kappa\frac{3T_N^k - 4T_{N-1}^k + T_{N-2}^k}{2\Delta r} = \gamma\left(T_N^k - T_a\right). \tag{C6}$$

From Equations (C4–C6), the prescribed boundary temperature T_N^k can be obtained.

Appendix D

FDM Algorithm for 2D Square

For 2D heat conduction in a square domain $[0, L] \times [0, L]$ with all boundaries subject to a convective heat flux boundary, the governing equation is given by,

$$\frac{\partial T}{\partial t} = \alpha\left(\frac{\partial^2 T}{\partial x^2} + \frac{\partial^2 T}{\partial y^2}\right), \tag{D1}$$

The boundary conditions are,

$$\begin{aligned} -k\left.\frac{\partial T}{\partial x}\right|_{x=0} &= \gamma\left[T(0,y,t) - T_a\right], & -k\left.\frac{\partial T}{\partial x}\right|_{x=L} &= \gamma\left[T(L,y,t) - T_a\right], \\ -k\left.\frac{\partial T}{\partial y}\right|_{y=0} &= \gamma\left[T(x,0,t) - T_a\right], & -k\left.\frac{\partial T}{\partial y}\right|_{x=L} &= \gamma\left[T(x,L,t) - T_a\right]. \end{aligned} \tag{D2}$$

and the initial condition is,

$$T(x, y, 0) = T_0. \tag{D3}$$

The second-order finite difference approximation for 2D heat equation is,

$$T_{i,j}^{k+1} = T_{i,j}^{k} + \alpha \Delta t \left(\frac{T_{i+1,j}^{k} - 2T_{i,j}^{k} + T_{i-1,j}^{k}}{\Delta x^2} + \frac{T_{i,j+1}^{k} - 2T_{i,j}^{k} + T_{i,j-1}^{k}}{\Delta y^2} \right). \tag{D4}$$

For the heat flux boundary conditions, we use a first-order finite difference approximation,

$$\begin{aligned}
&\text{At } x = 0: && \kappa \frac{3T_{2,j}^{k} - 4T_{1,j}^{k} + T_{0,j}^{k}}{\Delta x} = \gamma (T_{0,j}^{k} - T_a), \\
&\text{At } x = L: && \kappa \frac{3T_{N,j}^{k} - 4T_{N-1,j}^{k} + T_{N-2,j}^{k}}{\Delta x} = \gamma (T_{N,j}^{k} - T_a) \\
&\text{At } y = 0: && \kappa \frac{3T_{i,2}^{k} - 4T_{i,1}^{k} + T_{i,0}^{k}}{\Delta y} = \gamma (T_{0,i}^{k} - T_a), \\
&\text{At } y = L: && \kappa \frac{3T_{i,N}^{k} - 4T_{i,N-1}^{k} + T_{i,N-2}^{k}}{\Delta y} = \gamma (T_{N,i}^{k} - T_a).
\end{aligned} \tag{D5}$$